Aerodynamic Optimization and Fuel Burn Evaluation of a Transonic Strut-Braced-Wing Single-Aisle Aircraft

Timothy Chau* and David W. Zingg†
Institute for Aerospace Studies, University of Toronto, ON M3H 5T6

This paper presents an assessment of the potential fuel burn savings offered by the transonic strut-braced-wing configuration within the single-aisle class of aircraft relative to a modern conventional tube-and-wing through aerodynamic shape optimization based on the Reynolds-averaged Navier-Stokes equations. A representative strut-braced-wing aircraft is first developed through conceptual multidisciplinary design optimization based on the Airbus A320neo, with current technology levels assumed. A concept for the conventional tube-and-wing aircraft is also developed to represent the Airbus A320neo as a performance baseline. Single-point aerodynamic shape optimization is then performed on wing–body–tail models of each aircraft to address aerodynamic design challenges and to provide more accurate performance estimates. Results indicate that shock formation can be mitigated from the wing-strut junction of the strut-braced wing at Mach 0.78 and a relatively high design lift coefficient of 0.750, providing an 8.2% reduction in block fuel over a 1,000 nmi nominal mission when compared to the conventional tube-and-wing. Multipoint aerodynamic shape optimization is then performed to build toward a more credible estimate of fuel burn performance, with results showing a reduction in the fuel burn savings to 7.8% at the nominal design point relative to the conventional tube-and-wing to maintain a 7.6–8.0% improvement over the envelope of operating conditions, which includes design points at even higher Mach numbers and lift coefficients. These results demonstrate the viability of the transonic strut-braced-wing configuration for transport aircraft within the single-aisle class, and its potential for reducing commercial fleet fuel burn.

*Ph.D. Candidate, Institute for Aerospace Studies, University of Toronto, AIAA Member, tim.chau@mail.utoronto.ca
†Distinguished Professor of Computational Aerodynamics and Sustainable Aviation, Institute for Aerospace Studies, University of Toronto, AIAA Associate Fellow, dwz@utias.utoronto.ca

Nomenclature

b	=	Span
C_D	=	Drag coefficient
C_L	=	Lift coefficient
C_P	=	Pressure coefficient
c	=	Chord
D	=	Drag
$\mathcal{D}$	=	Design weights
$\mathcal{J}$	=	Objective function
L	=	Lift
L/D	=	Lift-to-drag ratio
M	=	Mach number
N	=	Number of grid nodes
S_{ref}	=	Reference area (gross)
T_{max}	=	Maximum thrust, SLS
t/c	=	Thickness-to-chord ratio
x,y,z	=	Cartesian coordinates
y^+	=	Nondimensional off-wall distance

Acronyms

CG	=	Center of Gravity
CTW	=	Conventional Tube-and-Wing
FFD	=	Free-Form Deformation
LE	=	Leading Edge
MAC	=	Mean Aerodynamic Chord
MDO	=	Multidisciplinary Design Optimization
MFW	=	Maximum Fuel Weight
MP	=	Multipoint
MTOW	=	Maximum Takeoff Weight
MZFW	=	Maximum Zero Fuel Weight
OEW	=	Operating Empty Weight

OML = Outer Mold Line

RANS = Reynolds-Averaged Navier-Stokes

SBW = Strut-Braced-Wing

SP = Single-Point

TE = Trailing Edge

TSFC = Thrust Specific Fuel Consumption

I. Introduction

With the demand for air travel projected to double in the next 15 years, researchers are seeking advanced aircraft and engine technologies that can dramatically reduce aviation fuel burn and CO_2 emissions. Toward this end, unconventional aircraft configurations [1] show much promise, with the potential to provide significant improvements to fuel efficiency through inherent advantages in aerodynamics, structures, and in some instances, propulsion, while remaining compatible with many other advanced technologies. Some configurations in discussion today include the blended or hybrid wing-body [2, 3], the joined [4] and box wings [5–7], the D8 [8], and the flying V [9]. Other examples include aircraft concepts with turbo- and hybrid-electric propulsion system architectures [10–12] and those with distributed propulsion systems [13]. Another concept is the truss-braced wing [14], whose compatibility with conventional fuselage and empennage designs positions it as a promising near- to mid-term option.

The primary advantage of the truss-braced-wing configuration comes from its 25–50% larger wing span, typically with aspect ratios ranging 16 to 20 as compared to the 9 to 11 of conventional wings, which enables substantial reductions in induced drag. This is supported by a structurally efficient truss topology consisting of a main strut and one or more jury struts, which can also be leveraged for a reduction in wing thickness, as well as an overall reduction in wing weight. With a thinner wing comes the benefit of reduced viscous and wave drag, with the latter also providing an opportunity for reducing wing sweep. This can further reduce the weight of the wing, while opening the possibility for natural laminar flow. A variant of the truss-braced wing is the strut-braced wing, which omits jury struts to favor a reduction in interference drag over some structural efficiency.

Given the integrated nature of the strut- and truss-braced-wing configurations, many studies have opted for the use of multidisciplinary design optimization (MDO) tools. For example, many of the earliest investigations performed by researchers at Virginia Tech and the Georgia Institute of Technology [15–19] involved comprehensive explorations of the conceptual design space through such tools, capturing trades between aerodynamics and structures, and the impact that these trades have on the overall sizing of a given aircraft concept. Single- and twin-aisle strut- and truss-braced-wing aircraft were investigated, with results indicating a significant potential for fuel savings. More recently, researchers have been focusing on the transonic aeroelastic behavior of these highly flexible wings [20, 21], and the impact of flutter on

their conceptual designs [22, 23], while other researchers are further investigating their conceptual designs with an emphasis on the structural design of their high aspect ratio wings [24].

Another concern that arises early in the preliminary design stage is the transonic channel effect caused by the narrow and sometimes enclosed regions surrounding the wing and struts, which extend beyond the capabilities of low-order aerodynamics models. This can cause the flow to accelerate and form shock waves, even at moderate transonic Mach numbers, potentially leading to boundary-layer separation and severe drag penalties. Given this potential impact, the PADRI workshop [25] was organized, which sought active and passive flow control strategies for addressing the transonic interference effects surrounding a Mach 0.72 strut-braced-wing geometry with a cruise lift coefficient of 0.406. Some of the more successful approaches involved the application of aerodynamic shape optimization based on the Reynolds-averaged Navier-Stokes (RANS) equations, which is capable of capturing and eliminating shock formation and boundary-layer separation in and around wing-strut junctions [26, 27]. RANS-based aerodynamic shape optimization was also applied by Li et al. [28] to design an aerodynamically efficient truss-braced-wing single-aisle aircraft at Mach 0.70 and a cruise lift coefficient of 0.770.

In order to demonstrate the viability of the strut- and truss-braced-wing configurations for commercial transport aircraft, however, such adverse effects must be addressed at higher and more conventional transonic Mach numbers where they are expected to be more difficult to address [29]. Although operating at lower transonic Mach numbers can be attractive for reducing fuel burn and emissions, it can also result in poor airline productivity due to increased direct operating costs [30], and incompatibilities with current airline operations. As such, researchers are now looking toward unconventional aircraft configurations designed for higher transonic Mach numbers, e.g. Mach 0.78–0.80 within the single-aisle class [31–33].

In a study done by Gagnon and Zingg [34], aerodynamic shape optimization based on the Euler equations was applied to the aerodynamic design of a Mach 0.78 strut-braced-wing regional jet based on the Bombardier CRJ-1000, which demonstrated that the shock waves within the wing-strut junction can be eliminated when considering only inviscid drag. Chau and Zingg [35] then showed that a low drag Mach 0.78 strut-braced-wing regional jet based on the Embraer E190-E2 can be achieved when accounting for trades between induced, viscous, and wave drag through aerodynamic shape optimization based on the RANS equations, even at a relatively high optimal cruise lift coefficient of 0.682. Based on a nominal range mission of 500 nmi, this strut-braced-wing aircraft was found to provide a relative fuel burn savings of 7.6% when compared to a similarly optimized Embraer E190-E2-like conventional tube-and-wing. Multipoint aerodynamic shape optimization was then applied to demonstrate that such low drag performance can be maintained when considering an envelope of flight conditions, which included design points at even higher Mach numbers and cruise lift coefficients [36]. The relative fuel burn performance was also maintained, ranging from 7.3 to 8.4% at the off-design conditions.

Relatively high cruise altitudes were also found to be necessary for achieving the cruise lift coefficients associated

with higher aerodynamic efficiency, as expected for wings with high aspect ratios [1, 37]. Indeed, for a given wing loading, operating at higher cruise altitudes re-balances the breakdown of induced and viscous drag, which tends toward the latter at conventional cruise altitudes. Favorable trades with climb and descent fuel were obtained, even with an initial cruise altitude of 44,670 ft. Given the relatively short operating ranges of regional jet aircraft, however, one can expect greater fuel burn savings for longer range aircraft, which spend a larger percentage of their flights at cruise.

One such type aircraft is the single-aisle class – a medium- to long-range aircraft class that has been of growing importance to the airline industry. According to the FAA, for example, single-aisle aircraft made up close to 50% of the US fleet in 2019, with the total number of single-aisle aircraft projected to grow by 35 aircraft per year [38]. Projections from Airbus also indicate that the A220 and A320 families are expected to comprise 76% of new deliverables from 2021 to 2040 for a total of 29,690 new aircraft [39].

Given the importance of the single-aisle market and the suitability of the strut- and truss-braced-wing configurations to the single-aisle class, many of the aviation industry's research efforts have focused on strut- and truss-braced-wing single-aisle aircraft. For example, Boeing and NASA have been investigating truss-braced-wing aircraft with the payload and range capabilities of a Boeing 737 MAX 8. This includes the Mach 0.70 Boeing SUGAR High [30] and Boeing SUGAR Volt [12], and more recently, the Boeing Transonic Truss-Braced Wing with Mach 0.745 [40] and Mach 0.80 [31, 32] variants. These efforts have been rewarded with the recently announced Sustainable Flight Demonstrator Project, which centers around a partnership between NASA and Boeing to develop a full-scale research aircraft of the Transonic Truss-Braced Wing by 2028 [41]. Other examples include studies done by ONERA, which investigate the advantages of a Mach 0.75 strut-braced-wing aircraft based on the mission requirements of the Airbus A320 [42], and a Mach 0.78 strut-braced-wing aircraft based on the Airbus A321 [33]. A Mach 0.72 strut-braced-wing aircraft similar to the Boeing SUGAR High was also investigated by DLR [43].

The studies presented in References [35, 36] demonstrate that efficient and robust strut-braced-wing regional jet aircraft can be designed at Mach 0.78 and design lift coefficients as high as 0.682 [35, 36], suggesting that this is also achievable for single-aisle aircraft, which typically operate at Mach numbers ranging 0.78–0.80. However, single-aisle aircraft prefer to operate at even higher cruise lift coefficients due in part to their higher design wing loadings. This can lead to elevated transonic interference effects surrounding the wing-strut junctions, which may result in higher costs in aerodynamic performance for removing them. Higher design cruise lift coefficients can also impose challenges toward aerodynamic performance robustness, translating to reduced drag divergence and buffet margins, or at the very least increased on-design performance compromises for maintaining a reasonable operating envelope [36]. Several system level differences between the single-aisle and regional jet classes must also be accounted for in order to obtain an accurate assessment of the fuel burn benefits offered by strut-braced-wing aircraft in the single-aisle class. For example, single-aisle strut-braced wings can achieve their optimum cruise lift coefficients at lower altitudes because of their higher wing loadings, thereby reducing mission climb fuel. Current single-aisle aircraft are also gate limited at 118 ft

wing spans, which implies higher weight penalties for strut-braced wings with a given relative span increase due to the extent of their folding wing tips. Single-aisle aircraft also have higher lift requirements, suggesting larger relative savings in induced drag, as well as longer range missions, as described previously.

The main objective of the present study, therefore, is to evaluate the relative fuel burn performance of a Mach 0.78 strut-braced-wing configuration within the single-aisle class when accounting for the transonic interference effects surrounding the wing-strut junction, trades between induced, viscous, and wave drag, and all system level trades relevant to a single-aisle variant. Aerodynamic shape optimization based on the RANS equations is introduced early in the preliminary design stage to address aerodynamic design challenges and to provide more accurate performance estimates relative to those obtained from a conceptual design environment similar to those of References [15–19]. Following the approach presented in Zingg et al. [44] and Chau and Zingg [35, 36], emphasis is placed on including first-order effects that have a significant impact on fuel burn performance through a judicious selection of the design considerations and fidelity levels required to model each discipline.

Current technology levels are assumed in order to focus on the benefits of the transonic strut-braced-wing configuration itself, given the uncertainties surrounding other advanced technologies that may or may not mature by the 2035–2040 timeframe. A conventional tube-and-wing concept representing the Airbus A320neo will also be developed and optimized to serve as a modern, notional best-in-class performance baseline. Although a year 2005 baseline aircraft could be selected to allow for assessments that align with international goals (see for example the studies done by Boeing [12, 30]), a year 2020 baseline aircraft is selected with the intent of maintaining a similar technology level across both aircraft. This is done in part to maintain consistency in the modeling of common aircraft components and subsystems. Examples include their fuselage designs, the structural layouts of their wing systems, the reference engines used to model their propulsion systems, and the various aircraft systems weight groups.

The paper is organized as follows. Section II presents the overall approach to evaluating the relative fuel burn benefit of the transonic strut-braced-wing single-aisle aircraft, while Section III provides an overview of each aircraft concept developed through low-order MDO. Section IV presents the problem setup for each high-fidelity aerodynamic shape optimization problem, with results from the single-point and multipoint optimization studies presented in Sections V and VI, respectively. Mach number and lift coefficient sensitivity studies are presented in Section VII, with conclusions presented in Section VIII.

II. Approach to Evaluating Fuel Burn Performance

In order to assess the relative fuel burn benefit of the transonic strut-braced-wing configuration for the single-aisle class of aircraft, this work follows a decoupled multifidelity multidisciplinary approach presented in Zingg et al. [44] and Chau and Zingg [35, 36], which supplements conceptual design with high-fidelity aerodynamic shape optimization to accurately capture trades between induced, viscous, and wave drag, including the adverse aerodynamic effects

unique to strut-braced wings. In this approach, careful consideration is made toward the various design and mission requirements of a given aircraft configuration of a given aircraft class and the disciplines needed to not only satisfy these requirements, but to also model the important physical effects that have a dominant effect on fuel burn performance. In this context, careful consideration must also be made toward the fidelity level of each discipline in order to avoid appreciable computational costs and problem complexity while capturing the relevant trends and tradeoffs.

Fuel burn performance is defined as the block fuel required to complete a nominal mission representing the most often flown mission of a given aircraft class. In principle, this is equivalent to the fuel burn performance of a given aircraft technology across a fleet of aircraft within a given class. In the present work, the strut-braced-wing configuration is evaluated for the single-aisle class based on the Airbus A320neo, which is selected to represent a notional best-in-class reference aircraft with current technology levels. This provides a nominal mission range and payload of 1,000 nmi and 165 passengers, respectively, with a cruise Mach number of 0.78. The relative fuel burn performance is then obtained by comparing the nominal mission block fuel of the strut-braced-wing single-aisle aircraft with that of a conventional tube-and-wing aircraft modeled to represent the Airbus A320neo as-drawn.

In the first phase of the decoupled approach, representative aircraft concepts are first developed through a conceptual MDO framework called Faber, which includes low- and medium-fidelity physics-based models and statistical correlations for sizing the weights of aircraft components and subsystems, and optimizing aircraft parameters and operating conditions. Faber provides a means for accounting for the majority of the top level aircraft requirements, which often involve various interdependencies across the different disciplines. Although the design problem of real aircraft can involve a prohibitive quantity of design considerations, many of the physical effects and interdisciplinary tradeoffs that have a first-order effect on fuel burn performance can be reasonably modeled with methods of lower fidelity levels. For example, for the conceptual design of transonic strut-braced-wing transport aircraft, some of the important first-order effects include:

- The induced drag savings offered by high aspect ratio wings
- The dependence of the aerodynamic efficiency of high aspect ratio wings on higher cruise lift coefficients, which is often achieved through higher cruise altitudes
- The dependence of wave drag on higher cruise lift coefficients
- The structural efficiency of strut-braced wing systems
- The weight penalties associated with high aspect ratio wings with reduced thickness
- The susceptibility of joined wing systems to global buckling under positive and negative load conditions
- The weight penalties associated with wing folding mechanisms for wing spans that exceed a given gate limit
- The fuselage weight penalties associated with high-wing configurations
- The weight penalties associated with increased cabin pressurization loads when operating at high cruise altitudes
- The dependence of thrust available on cruise altitude
- The dependence of climb and descent fuel weight on cruise altitude

These factors are accounted for in the conceptual design of the strut-braced-wing single-aisle aircraft, where the objective of the optimization problem is to drive the aircraft parameters and operating conditions toward a minimum fuel burn solution, while maintaining a feasible concept. Design variables are included to size the wing, strut, horizontal and vertical tails, and propulsion systems, as well as to optimize the initial cruise altitude of each design mission.

Some design parameters are omitted, however, including wing span, wing sweep, and the attachment location of the wing-strut junction, whose optimizations are considered beyond the capabilities of the low-order models. For instance, obtaining the optimal tradeoff between aerodynamic and structural performance for wing span and wing sweep is likely to require higher fidelity aerostructural analysis and optimization methods. It is also likely that parameters such as wing span are largely driven by transonic aeroelastic effects such as flutter, which also extends beyond the scope of the current work. As such, these design parameters are carefully selected and set based on similar transonic strut- and truss-braced-wing single-aisle aircraft found in the literature which have been subjected to more extensive preliminary design efforts (see for example Bradley et al. [30]).

These aircraft concepts are then used in the second phase of the decoupled approach to develop wing–body–tail models of each aircraft for high-fidelity aerodynamic shape optimization. Through a RANS-based aerodynamic shape optimization framework called Jetstream, a more detailed aerodynamic design of the wing and tail systems is performed, which accounts for shock formation, boundary-layer separation, and nonlinear interference effects, providing a means for addressing the transonic interference effects experienced by high-speed strut-braced-wing aircraft. Here, the objective is to minimize the nominal mission cruise drag, under the assumption that non-aerodynamics and non-cruise contributions to fuel burn remain approximately constant to first order. Several practical constraints are included to minimize the impact of aerodynamic shape optimization on non-aerodynamics disciplines, such as minimum wing thickness and volume constraints based on the conceptual designs of each aircraft.

Single-point optimization is first performed to obtain a baseline set of results, and to provide a sense for the design features that are favorable when off-design performance compromises are not necessary. Multipoint optimization is then performed to determine if a robust aerodynamic design can be achieved over a range of suitable cruise conditions, more true to the design of a real aircraft. Moreover, multipoint optimization is performed in order to determine if the relative fuel burn benefit offered by the transonic strut-braced-wing single-aisle aircraft is robust to more challenging cruise conditions that include higher Mach numbers or lift coefficients. The nominal mission block fuel of each aircraft is then re-evaluated through a synthesis of low- and high-fidelity performance estimates.

An overview of the conceptual design environment is presented in Appendix A, while Appendix B provides an overview of the high-fidelity aerodynamic shape optimization framework. For a more detailed account of the conceptual design problem of each aircraft, see Appendix C.

III. Aircraft Concepts and Characteristics

The aircraft concepts developed through conceptual MDO, herein referred to as the CTW160 and SBW160 for the conventional tube-and-wing and strut-braced-wing single-aisle aircraft, respectively, are shown in Figure 2. The resulting aircraft characteristics are presented in Table 1. For the CTW160, the design weights agree well with those of the Airbus A320neo, which has an MTOW of 174,200 lb, MZFW of 141,800 lb, OEW of 97,700 lb, and MFW of 46,243 lb. This agreement is due in part to careful calibrations of the weight groups, which are maintained in the modeling of the SBW160 for consistency.

For the SBW160, a 30.0% larger wing span and 73.9% higher wing aspect ratio leads to a 19.2% higher cruise L/D and 17.7% lower cruise drag for the nominal range mission when compared to the CTW160. It is important to note, however, that the SBW160 must operate at a much higher initial cruise altitude of 42,220 ft, which translates to a cruise C_L of 0.750. As described in Appendix C, this corresponds to an active maximum cruise C_L constraint. Note that this represents a substantially higher design C_L than that of the strut-braced-wing regional jet of Chau and Zingg [35, 36] at 0.682, making for a more challenging aerodynamic design problem.

Even with a relatively high wing aspect ratio, and the weight penalties associated with the wing folding mechanism, the weight of the SBW160's wing system is 16.5% less than that of the CTW160. This can be attributed to the structural efficiency of the strut-braced wing topology, as well as the advantages of a composite construction. In the present work, composite wing structures are modeled with Boeing's advanced quasi-isotropic composite material [30] based on the conceptual design studies done by Chakraborty et al. [19], and is considered a current and readily available technology.

Between the two aircraft, the weight of the tail systems are similar, although the weight of the horizontal tail is 24.2% less for the SBW160 than that of the CTW160. This comes in part from the larger moment arm provided by the T-tail configuration, which results in a reduced horizontal tail area necessary for achieving the target volume ratio. The larger moment arm, however, leads to higher fuselage bending loads captured by the empirical equations, which translate to a heavier fuselage. In particular, the weight of the fuselage is 16.6% higher for the SBW160 relative to that of the CTW160, which can also be attributed to the weight penalties associated with high-wing configurations and fuselage-mounted landing gear systems.

With regard to the propulsion systems, the podded engines are of a similar size. More specifically, the maximum takeoff thrust of the SBW160 is only 3.0% less than that of the CTW160. This translates to a negligible reduction in cruise TSFC.

Accounting for aerodynamics, weight, and propulsion, overall reductions in the design weights of the SBW160 are achieved relative to those of the CTW160. For example, MTOW, MZFW, and OEW are reduced by 3.1%, 1.1%, and 1.6%, respectively. MFW is also reduced by 12.9%, indicating the potential savings offered by the SBW160 over longer ranges where a larger portion of the mission profile is allocated to cruise. With respect to the nominal range mission, the low-order models indicate that the SBW160 can offer a 10.9% savings in block fuel when compared to the fuel burn

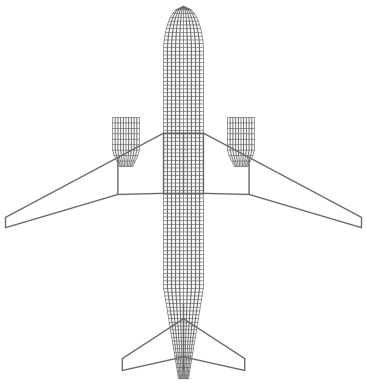

(a) CTW160

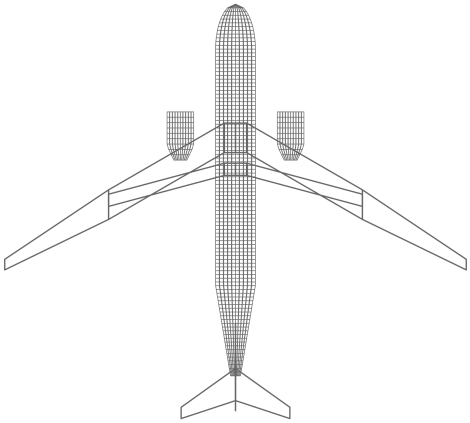

(b) SBW160

Fig. 2 Aircraft concepts developed through conceptual MDO.

Table 1 Aircraft characteristics from conceptual MDO.

Parameter	CTW160	SBW160
Reference MAC [ft]	13.70	8.90
Reference area [ft^2]	1,332	1,288
Span [ft]	118.0	153.0
Sweep (LE) [deg]	28.0	30.0/33.8
Aspect ratio [–]	10.45	18.17
Wing loading [lb/ft^2]	131.1	131.1
Thrust-to-weight ratio [–]	0.311	0.311
MTOW [lb]	174,280	168,830
MZFW [lb]	142,090	140,560
OEW [lb]	97,990	96,460
Fuselage [lb]	17,840	20,800
Wing [lb]	18,710	15,620
Horizontal tail [lb]	1,860	1,410
Vertical tail [lb]	1,080	1,450
Nacelle and pylon [lb]	3,630	3,530
Landing gear [lb]	6,570	6,370
Propulsion [lb]	16,270	15,800
Systems [lb]	24,540	24,330
Operational items [lb]	5,050	5,050
Unusable fuel [lb]	2,440	2,120
MFW [lb]	45,970	40,030
Maximum payload [lb]	44,100	44,100
Max T/O thrust (per eng.) [lb]	27,080	26,280
Cruise TSFC [lb/lb/hr][1]	0.5340	0.5346
Mach number[1] [–]	0.78	0.78
Initial cruise altitude[2] [ft]	35,000	42,220
Reynolds number[1] [$\times 10^6$]	25.58	11.90
Cruise L/D[1] [–]	17.7	21.1
Cruise C_L[1] [–]	0.524	0.750
Cruise C_D[1] [–]	0.0296	0.0356
Cruise drag[1] [lb]	8,350	6,870
Block fuel[2] [lb]	11,580	10,320

[1]With respect to the start of cruise for the nominal range mission.

[2]With respect to the nominal range mission.

performance of the CTW160.

IV. High-Fidelity Aerodynamic Shape Optimization Problem Setups

This section presents the setup for each high-fidelity aerodynamic shape optimization problem. The baseline geometries are first presented, which are created based on the aircraft concepts described in the previous section. The computational grids are then presented, which includes the optimization level grids, as well as the finer grid levels used to perform grid convergence studies following optimization. The single-point and multipoint optimization problem formulations then follow, which include descriptions of the objective functions, design variables, and constraints.

A. Baseline Geometries

High-fidelity wing–body–tail models of each aircraft are created based on the conceptual designs presented in Section III. These 3D models provide a means for optimizing each wing and tail system while capturing the dominant aerodynamic effects, including the lift and interference drag contributions from the fuselage, at a reasonable computational cost. For both aircraft, the fuselage nose and tail sections are modeled based on the modern OML design of the Airbus A220-300 [45]. For the CTW160, the wing-fuselage fairing is also designed based on the Airbus A220-300 [45], while the wing- and strut-fuselage fairings of the SBW160 are based on those of the PADRI geometry [25]. These are repositioned along the fuselage in reference to the high-speed concepts presented in Bradley et al. [30].

For both aircraft, the baseline wing designs are generally untwisted and defined by RAE-2822 airfoil profiles, which offer suitable transonic performance from which to begin each gradient-based optimization. For the SBW160, the baseline strut design is also untwisted and defined by symmetric supercritical SC(2)-0012 sections since the strut is initially assumed to be non-lifting. The horizontal tail sections of each aircraft are defined by SC(2)-0010 profiles that are maintained throughout the optimization process.

B. Computational Grids

Structured multiblock grids are developed for each wing–body–tail geometry with O-H blocking topologies that include the necessary patches surrounding the junctions of the wing and strut, wing and fuselage, strut and fuselage, and wing and horizontal tail for accommodating the patch-based deformation schemes presented in Osusky et al. [46] and Chau and Zingg [35]. Optimization is performed on the L0 grid level presented in Table 2, which is based on the *medium mesh* resolution of the Fourth Drag Prediction Workshop (DPW) gridding guidelines [47]. Post-optimization, grid convergence studies are performed using the L1 and L2 grid levels in addition to L0 to obtain estimates of the grid-converged C_D values, i.e. in the limit of an infinitely fine grid, via Richardson extrapolation [48]. Assuming that

Table 2 Grid information. Single-point (SP) and multipoint (MP) optimizations are performed on the L0 grid level, while the L1 and L2 grid levels are used in addition to L0 for performing grid convergence studies.

Grid	Number of Nodes	Avg. Off-wall Spacing[1]	Avg. y^+ (SP)	Avg. y^+ (MP)[2]
		Conventional Tube-and-Wing		
L0	14.41×10^6	8.31×10^{-7}	0.574	0.568
L1	27.56×10^6	6.50×10^{-7}	0.436	0.432
L2	54.85×10^6	5.04×10^{-7}	0.331	0.328
		Strut-Braced Wing		
L0	26.51×10^6	1.71×10^{-6}	0.573	0.570
L1	50.50×10^6	1.34×10^{-6}	0.439	0.437
L2	99.54×10^6	1.04×10^{-6}	0.336	0.335

[1]Off-wall spacings are in units of mean aerodynamic chord.
[2]Mean of the average values across each set of design points.

the grids are in the asymptotic region and that convergence is monotonic, the numerical order of accuracy is given by

$$p = \frac{1}{\ln r} \ln\left(\frac{|f_0 - f_1|}{|f_1 - f_2|}\right) \tag{1}$$

where f_0, f_1, and f_2 are the aerodynamic functionals on grid levels L0, L1, and L2, respectively, and r is the ratio of grid spacings from one grid level to another. The grid-converged estimate can then be obtained through

$$f_\infty \approx f_2 + \frac{f_2 - f_1}{r^p - 1} \tag{2}$$

The grid levels are generated automatically with refinement factors, r, of approximately two and four relative to L0, for L1 and L2, respectively, through the mesh parameterization scheme described in Appendix B. Some of the grid convergence studies are presented in more detail later in Section VI. Figure 3 illustrates the surface meshes and patch topologies for each wing–body–tail geometry.

C. Single-Point Optimization Problem Formulations

The objective of each single-point optimization problem is to minimize cruise drag, namely, $\mathcal{J} = C_D$, while subject to constant lift and zero pitching moment constraints for maintaining steady level flight. Design variables include angle of attack, twist, and section shape degrees of freedom, which are presented in Table 3 along with their lower and upper bounds. Planform design variables such as the taper, sweep, span, and dihedral degrees of freedom described in Appendix B are assumed to have a strong dependence on non-aerodynamics disciplines and off-design conditions (e.g. structures, stability and control, and takeoff and landing), and so are not considered in the present work.

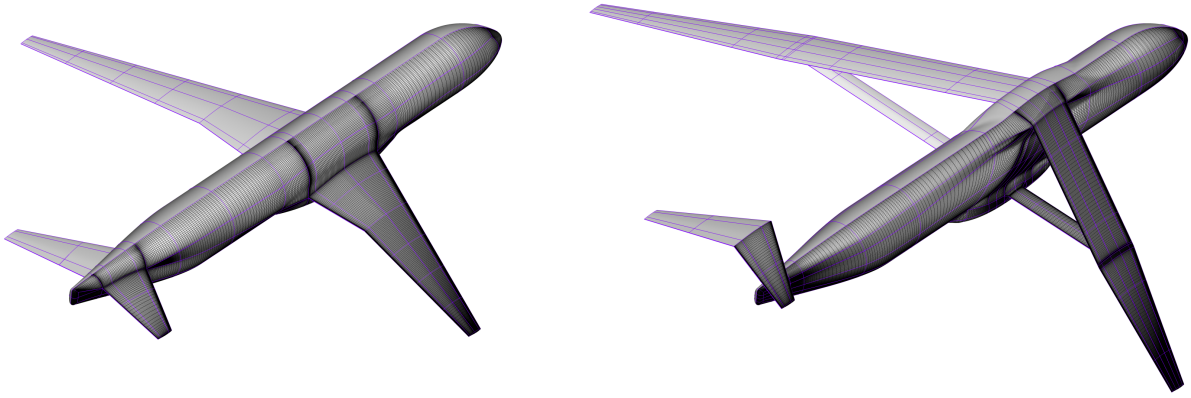

(a) CTW160 **(b) SBW160**

Fig. 3 Optimization level surface meshes (black lines) and patch topologies (purple lines) for the initial geometries.

Table 3 Design variable information for single-point aerodynamic shape optimization.

Design Variable	Quantity		Lower Bound	Upper Bound
	CTW160	SBW160		
Angle of attack	1	1	−3.0°	+3.0°
Twist[1,2]	16	42	−10.0°	+10.0°
Wing	12	19	−10.0°	+10.0°
Strut	–	19	−10.0°	+10.0°
Horizontal tail	4	4	−10.0°	+10.0°
Section shape	264	836	0.5	2.0
Wing	264	418	0.5	2.0
Strut	–	418	0.5	2.0
Horizontal tail	0	0	0.5	2.0
Total	**281**	**879**	–	–

[1]SBW160 wing root and vertical strut twist bounds are limited to ±3.5°.

[2]Twist design variables are used to define the horizontal tail incidence degrees of freedom.

Figure 4 shows the free-form and axial deformation geometry control system for each aircraft optimization. The free-form deformation (FFD) volumes are cubic in the parametric spanwise and chordwise directions, and linear in the parametric vertical direction, providing smooth deformations between each FFD-volume cross-section and their control points. The axial curves are positioned at the quarter chord of the primary and secondary lifting surfaces.

For the CTW160, the main wing is embedded within an FFD volume with 12 FFD-volume cross-sections, each with 11 FFD-volume control points above and below the aerodynamic surfaces, distributed uniformly in the parametric chordwise direction. For the SBW160, the main wing is also embedded within an FFD volume with the same number of FFD-volume cross-sections per unit span, each also with 11 FFD-volume control point pairs. In order to provide the

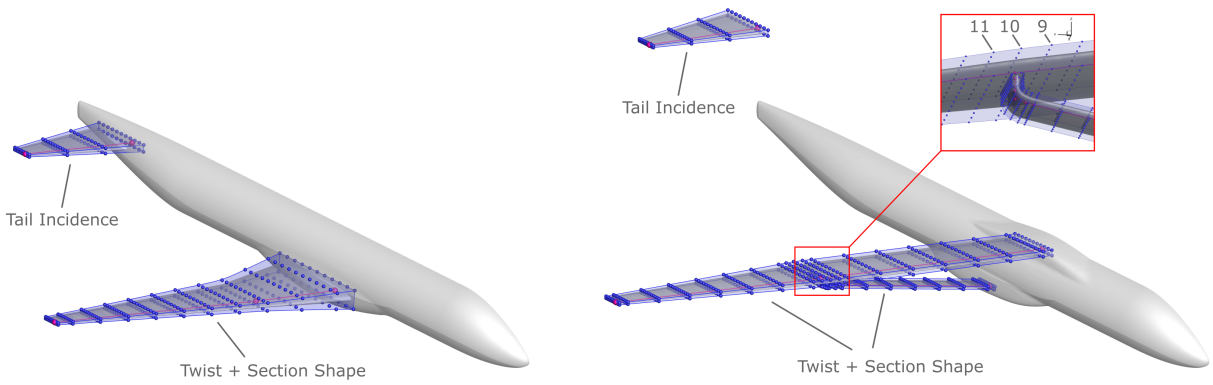

(a) CTW160 **(b) SBW160**

Fig. 4 Geometry control systems with FFD volume (blue) and axial curve (fuschia) entities. The 9th, 10th, and 11th wing FFD-volume cross-sections used in the twist interpolation constraint are labeled.

optimizer with the geometric freedom necessary for addressing the transonic interference effects, however, additional FFD-volume cross-sections are introduced near the wing-strut junction, resulting in 19 FFD-volume cross-sections. Three additional FFD volumes are also included to individually embed the main, blended transition, and vertical struts, as shown in the inset of Figure 4b, which provide an additional nine, five, and five unique FFD-volume cross-sections, respectively, for a total of 19 FFD-volume cross-sections.

The horizontal tail of each aircraft is also embedded within an FFD volume to provide incidence angle control. This is achieved by introducing a linear constraint to link the twist design variables across the four FFD-volume cross-sections. For the SBW160, several linear constraints are also introduced to prevent excessive waviness in the regions surrounding the wing and strut. These include a twist interpolation across the 9th, 10th, and 11th wing FFD-volume cross-sections positioned at the wing-strut junction, a twist interpolation across the blended transition strut, and a linking of the twist design variables across the vertical strut.

Other linear constraints include fixed leading and trailing edge constraints and minimum t/c scaling constraints. The former sets equal the section shape design variables of the lower and upper FFD-volume control points for the first and last pairs of each FFD-volume cross-section; this prevents the FFD-volume cross-sections from being sheared, namely, introducing shear twist, and also prevents translations of the free-form and axial deformation geometry control system by anchoring the leading-edge points to the axial curves. The latter places a minimum bound on the vertical separation between each pair of FFD-volume control points, which also prevents crossovers of the FFD-volume control points.

Although the twist and section shape degrees of freedom are assumed to have a lesser dependence on non-aerodynamics disciplines and off-design conditions, nonlinear constraints are still necessary to help maintain feasible concepts. This includes a minimum volume constraint, which places a minimum bound on the wing, and wing and strut OML volumes of the CTW160 and SBW160, respectively, in order to ensure that there is sufficient volume to contain the fuel tanks that must store the maximum fuel weight. These bounds account for utilization factors and unusable fuel.

Minimum $(t/c)_{\max}$ constraints are also included across the wing, and wing and strut of the CTW160 and SBW160, respectively. In conjunction with the minimum volume constraint, the minimum $(t/c)_{\max}$ constraints serve as surrogates for maintaining a minimum structural depth based on stiffness distributions provided by the medium-fidelity structural sizing and analysis described in Appendix A. Note that the minimum t/c scaling constraint bounds are more relaxed than those of the minimum $(t/c)_{\max}$ constraints. This allows the optimizer to shift the location of $(t/c)_{\max}$ along the chord when the minimum $(t/c)_{\max}$ constraint is active at a given wing section. Table 4 provides a summary of the linear and nonlinear constraints included for each optimization problem.

D. Multipoint Optimization Problem Formulations

In order to investigate whether the advantages in aerodynamic performance and fuel efficiency offered by the SBW160 can be maintained when considering a suitable range of cruise conditions, a five-point stencil is considered as per Chau and Zingg [36], which places emphasis on operating conditions that are deemed challenging for the strut-braced-wing configuration. Included are the nominal design point, two design points at Mach 0.78 and ±10% nominal C_L, and two design points at Mach 0.81 and −10% and −20% nominal C_L. The objective is then given by a weighted sum of the cruise drag, namely,

$$\mathcal{J} = \sum_{i=1}^{5} \mathcal{D}(M_i, C_{L_i})\, C_D(M_i, C_{L_i}) \tag{3}$$

where $\mathcal{D}(M_i, C_{L_i})$ are user-specified design weights. In aircraft design, such design weights can be selected based on statistical distributions that indicate the number of flights operating under each specific flight condition. However, such data are not always accessible or readily available particularly for future aircraft. Therefore, it is reasonable and sufficient to assume that the nominal design point has a more substantial priority over the remaining operating conditions. In the present work, a two-fold priority is assumed for the on-design operating condition, with the off-design operating conditions weighted equally. Table 5 provides a summary of the operating conditions and their design weights.

The design variables and constraints for the multipoint optimization problems are the same as those of the single-point optimizations presented in Tables 3 and 4, respectively. However, the constant lift constraints are set for each design point based on the C_L requirements provided in Table 5. Since flight control surfaces such as elevators are not modeled in the present work, which are sometimes used with variable incidence horizontal tails to trim a given aircraft at off-design cruise conditions, the pitching moment constraint is only enforced for the nominal design point.

V. Single-Point Optimization Studies

Single-point optimized designs of the CTW160 and SBW160 are obtained following 135 and 126 function evaluations, respectively. Each optimization is considered complete when the objective function (C_D) has converged, feasibility—a

Table 4 Constraint information for single-point aerodynamic shape optimization.

Constraint	Quantity		Description
	CTW160	SBW160	
Lift	1	1	Constrains the aircraft lift to equal the weight at the start of cruise (nonlinear)
Trim	1	1	Constrains the aircraft pitching moment to equal zero (nonlinear)
Minimum volume	1	1	Constrains the minimum wing (and strut) OML volume based on fuel storage requirements (nonlinear)
Minimum $(t/c)_{\max}$	10	30	Minimum maximum thickness-to-chord ratio constraints based on structural requirements (nonlinear)
Minimum t/c scaling	132	418	Constrains the local vertical separation between each pair of FFD-volume control points to be greater or equal to 50% of its initial value (linear)
Fixed LE/TE	24	76	Constrains section shape design variables at the leading- and trailing-edges to be equal and opposite between the lower and upper FFD-volume control points (linear)
Linear junction wing twist	0	1	Interpolates the twist design variables across the 9th and 11th wing FFD-volume cross-sections.
Linked horizontal tail twist	1	1	Links the twist design variables of the horizontal tail to translate to incidence angle control (linear)
Linked vertical strut twist	0	1	Links the twist design variables of the vertical strut segment (linear)
Linear transition strut twist	0	1	Interpolates the twist design variables across the transition strut segment (linear)
Total	**170**	**531**	–

Table 5 Single-point and multipoint optimization design weights and operating conditions.

Design Point	$\mathcal{D}$	M	C_L	
			CTW160	SBW160
SP1	1	0.78	0.524	0.750
MP1	1/3	0.78	0.524	0.750
MP2	1/6	0.78	0.576	0.825
MP3	1/6	0.78	0.472	0.675
MP4	1/6	0.81	0.472	0.675
MP5	1/6	0.81	0.419	0.600

measure of constraint violations—has reduced to 10^{-5} or less, and optimality has reduced by one to two orders of magnitude. Although a deeper convergence of optimality is preferred, optimization problems of this complexity often do not yield substantial improvements to the objective when permitted to continue further. At each optimum, the angle of attack is at its upper bound of 3°, and the minimum volume and $(t/c)_{\max}$ constraints are active, with the exception of some of the minimum $(t/c)_{\max}$ constraints over the outboard portion of the SBW160's wing.

Table 6 presents the estimates of aerodynamic performance and fuel burn for each optimized aircraft. Based on grid-convergence studies performed for each optimized wing–body–tail model, the optimized SBW160 has the advantage of a 10.6% higher cruise L/D and an 11.5% lower cruise drag relative to the optimized CTW160. Full aircraft performance is obtained by introducing a 5% markup on skin friction drag to approximate contributions from airframe excrescences, and low-order estimates of the drag contributions from the vertical tails, nacelles, and pylons. This provides the optimized SBW160 with a 13.0% higher cruise L/D and a 13.5% lower cruise drag relative to the optimized CTW160. Note that these drag contributions are greater for the CTW160 due to its lower cruise altitude, which translates to higher viscous drag, as well as its relatively larger horizontal and vertical tails. Supplementing these results with approximations for the start of cruise weight and TSFC of each aircraft, and introducing low-order estimates of the fuel required for warmup, taxi, takeoff, climb, descent, and landing, the single-point optimized SBW160 is found to provide an 8.2% savings in block fuel over the nominal range mission relative to the similarly optimized CTW160.

The initial and optimized spanwise lift distributions are shown in Figure 5. For the CTW160, the optimized spanwise lift distribution is elliptical in form when summing the contributions from the wing (and fuselage) and horizontal tail, but features an inboard shift to avoid trim and wave drag penalties that can come from high outboard wing loading. Similar trends can be seen for the optimized spanwise lift distribution of the SBW160. However, the inboard shift is more pronounced due to the larger wing span, which, at a similar wing sweep leads to an increased nose-down pitching moment per unit outboard wing loading. The much higher cruise C_L of the SBW160, along with its smaller chord lengths, can also lead to relatively high outboard sectional lift coefficients that can result in increased wave

Table 6 Single-point optimized aircraft performance at the nominal design point.

Parameter	CTW160	SBW160	Δ
	High Fidelity[1]		
L/D [–]	21.71	24.00	+10.6%
C_L [–]	0.524	0.750	+43.1%
C_D [–]	0.0241	0.0312	+29.4%
Lift [lb]	148,040	144,770	−2.2%
Drag [lb]	6,970	6,170	−11.5%
	Low and High Fidelity[2]		
L/D [–]	18.66	21.09	+13.0%
C_L [–]	0.524	0.750	+43.1%
C_D [–]	0.0281	0.0356	+26.6%
Lift [lb]	148,040	144,770	−2.2%
Drag [lb]	7,930	6,870	−13.5%
Block fuel [lb]	11,490	10,550	−8.2%

[1]Includes wing (and strut), fuselage, and horizontal tail contributions.

[2]Includes a 5% excrescence drag markup, and profile drag contributions from the vertical tail, nacelles, and pylons.

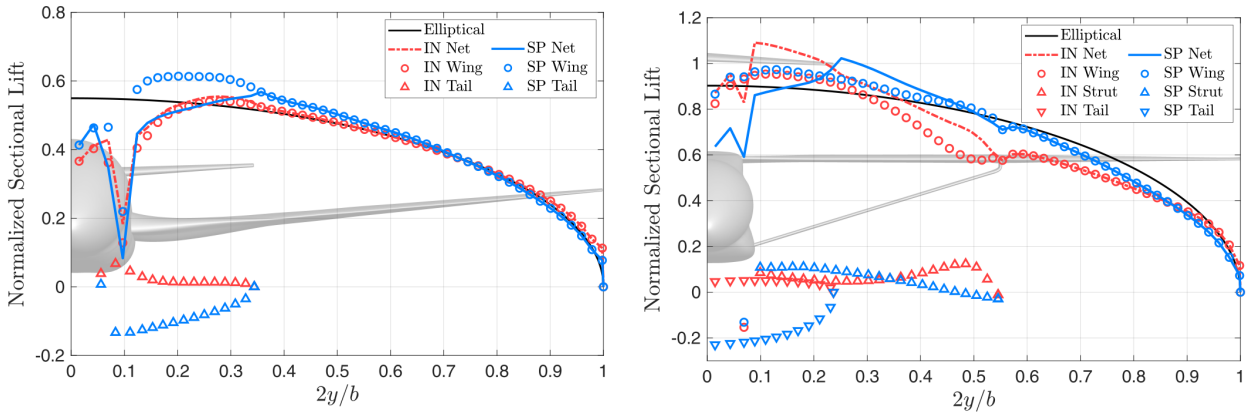

(a) CTW160 **(b) SBW160**

Fig. 5 Initial and single-point optimized spanwise lift distributions computed on the L0 grid level at the nominal design points.

drag. The SBW160 also features a lifting strut toward the wing root, which allows for a decrease in the inboard wing loading and hence sectional lift coefficients [35]. The strut also produces a modest quantity of negative lift toward the wing-strut junction, compensated locally by the wing, to alleviate the adverse pressure gradients found within those regions [27, 35, 49].

The overall flow characteristics of the optimized CTW160 are shown in Figure 6. From Figure 6a, it can be seen

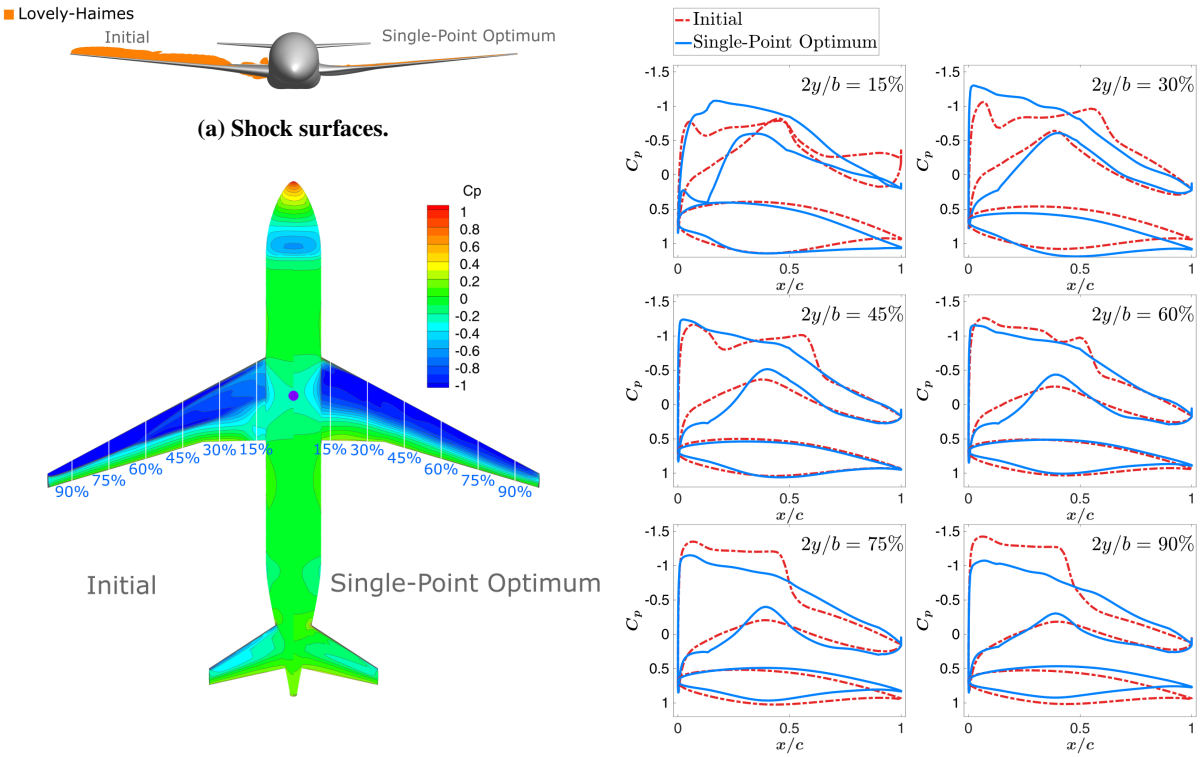

(a) Shock surfaces.

(b) Surface pressure contours and CG (purple circle).

(c) Airfoil profiles and pressure distributions.

Fig. 6 CTW160: Initial and single-point optimized design and flow features. Flow features are computed on the L0 grid level at $M = 0.78$ and $C_L = 0.524$.

that the initial shock surfaces approximated by the Lovely-Haimes detection method are all but eliminated following optimization. This is consistent with the smooth pressure distributions over the suction side of the wing, as illustrated in Figures 6b and 6c. The isobars are also well-aligned with the geometric sweep of the wing, indicating good wave drag performance.

An equivalent set of results are shown in Figure 7 for the optimized SBW160. As with the CTW160, the shock surfaces present over the initial wing design are largely removed post-optimization. Although residual shock surfaces appear to remain, the upstream Mach numbers are of Mach 1.1 or less, indicating that they are weak and contribute little to drag. Indeed, this is confirmed by the smooth optimized pressure distributions shown in Figure 7c, especially toward the wing root. This also agrees well with the features illustrated in Figure 7b, namely, smoothly varying surface pressures and isobars aligned with the geometric sweep of the wing.

Figure 8a shows the initial and optimized surface pressure contours surrounding the wing-strut junction. These are accompanied by airfoil profiles and pressure distributions shown in Figure 8b, which have been extracted normal to the axial curves and along the parametric spanwise direction. These wing sections include geometric twist, but not angle of attack as included in the previous pressure distributions. Within the initial wing-strut junction, sudden changes in the surface pressure contours can be observed, which have been smoothed out post-optimization. From the initial pressure

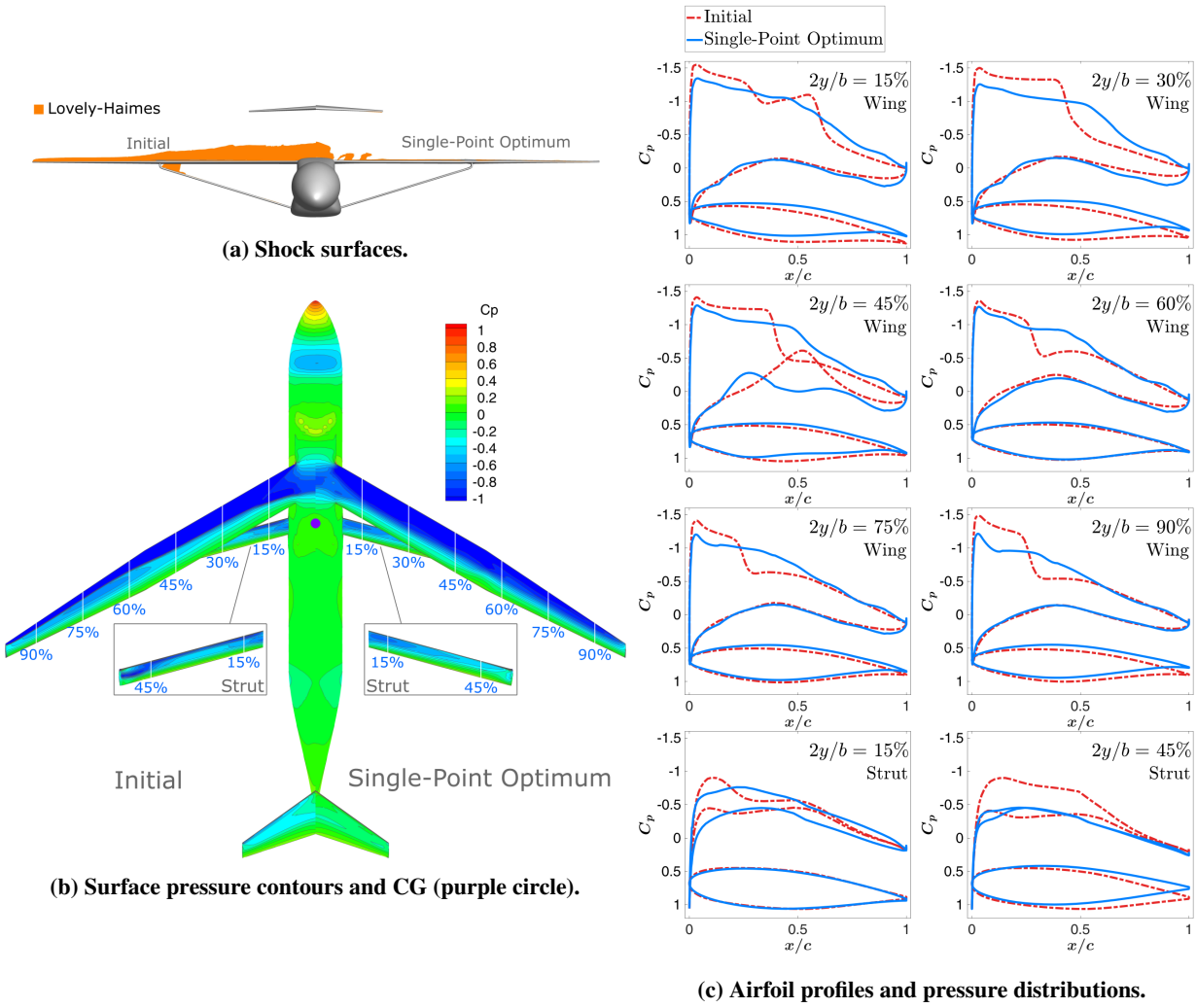

(a) Shock surfaces.

(b) Surface pressure contours and CG (purple circle).

(c) Airfoil profiles and pressure distributions.

Fig. 7 SBW160: Initial and single-point optimized design and flow features. Flow features are computed on the L0 grid level at $M = 0.78$ and $C_L = 0.750$.

distributions, it can be seen that these are the result of rapid decreases in local pressure caused by the transonic channel effect. This leads to the formation of shock waves as indicated by the rapid increases in local pressure that follow. Such adverse effects are addressed by the optimizer through novel bump-like features over the lower surface of the wing, which reduce the pressure peaks present over the lower surface of the initial wing geometry [35]. This is supported by an outwards twist distribution over the strut, which simultaneously mitigates the pressure peaks over the inner surface of the initial strut geometry [35]. Overall, the outwards force distribution surrounding the wing-strut junction leads to a minimum induced drag solution [50].

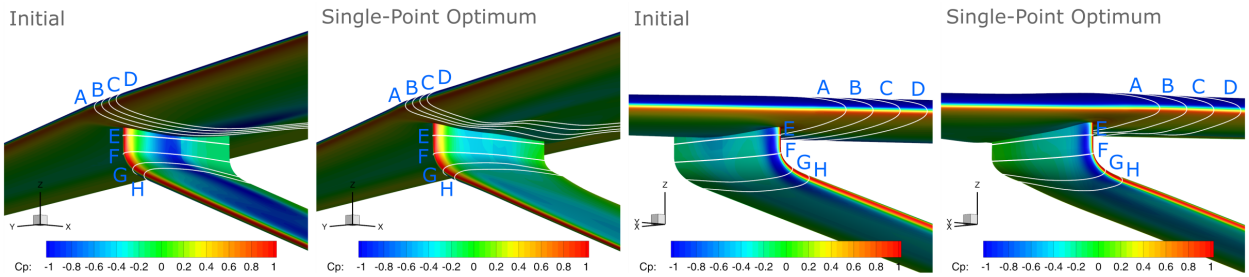

(a) Surface pressure contours.

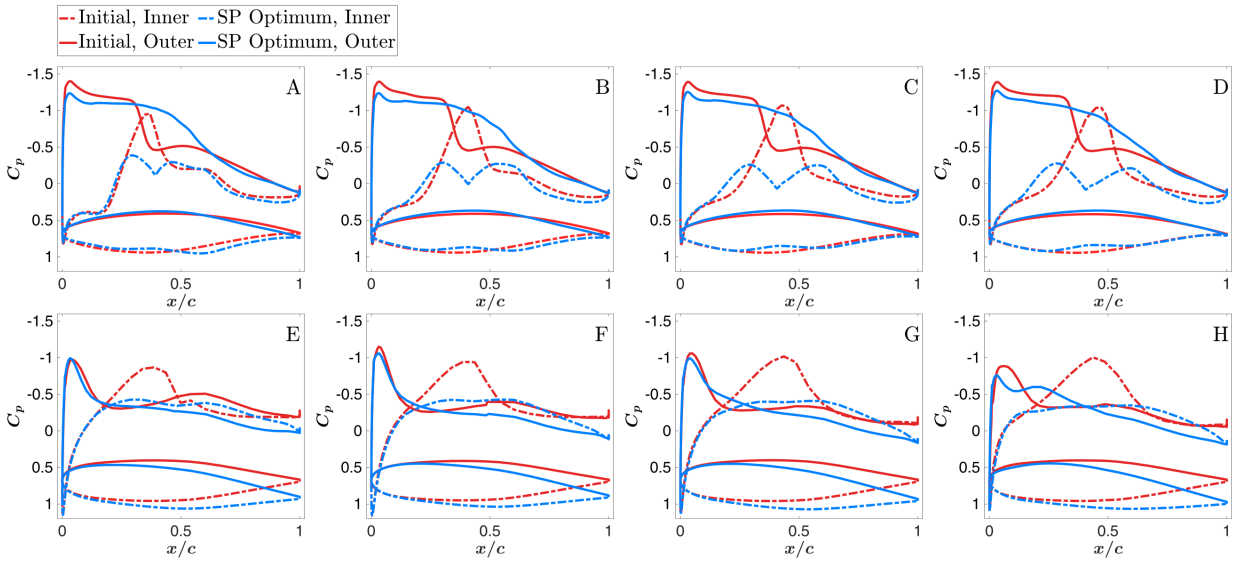

(b) Airfoil profiles and pressure distributions.

Fig. 8 SBW160: Initial and single-point optimized surface pressure contours with inner [(a),left] and outer [(a),right] views of the strut, and pressure distributions at different stations along the wing and strut. Results are computed on the L0 grid level at $M = 0.78$ and $C_L = 0.750$.

VI. Multipoint Optimization Studies

Starting from the design variables obtained from single-point optimization, multipoint optimized designs are obtained following 58–61 function evaluations (i.e. evaluations of Equation 3), with more than 95% of the weighted drag reductions achieved after the first 29–31 function evaluations. Grid convergence studies performed for each design point of the CTW160 and SBW160 are shown in Figure 9, which includes both single-point and multipoint optimums. Overall, convergence in C_D is monotonic and consistent across all grid levels for both aircraft, suggesting that the grid resolution of the L0 grid level is sufficient for optimization. Richardson extrapolation provides objective function values of 254 and 242 drag counts for the single-point and multipoint optimized CTW160, respectively, while for the single-point and multipoint optimums of the SBW160, these correspond to 329 and 318 drag counts, respectively.

Table 7 presents a summary of the aircraft performance for the multipoint optimized CTW160 and SBW160, with the results from the single-point optimizations included for comparisons. With regard to the high-fidelity wing–body–tail

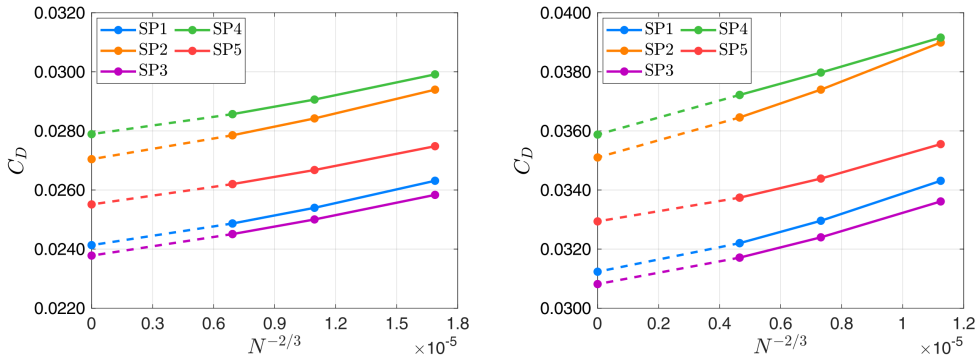

(a) CTW160 single-point optimum.

(b) SBW160 single-point optimum.

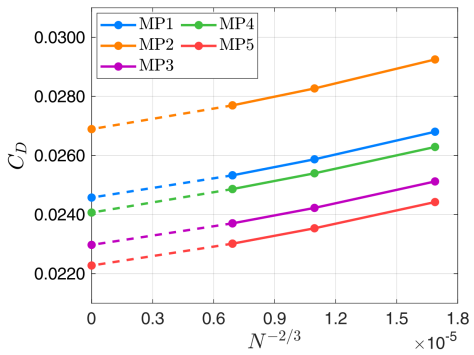

(c) CTW160 multipoint optimum.

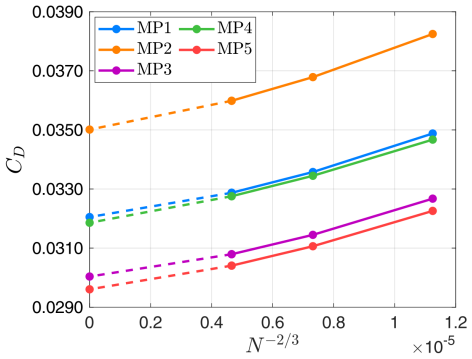

(d) SBW160 multipoint optimum.

Fig. 9 Grid convergence studies for the single-point and multipoint optimized single-aisle aircraft geometries at constant lift, evaluated at each of the five design points. Drag coefficients at $N^{-2/3} \rightarrow 0$ are obtained from Richardson extrapolation.

models of each aircraft, results indicate that the multipoint optimized SBW160 offers a 9.7% higher cruise L/D and a 10.9% lower cruise drag for the nominal range mission, when compared to the multipoint optimized CTW160. Constructing the full aircraft performance as before, the advantage of the multipoint optimized SBW160 becomes a 12.2% improvement in cruise L/D and a 12.8% reduction in cruise drag. These translate to a 7.8% fuel burn savings for the single-aisle class when comparing the block fuel of each multipoint optimized aircraft.

Figure 10 shows a comparison of the grid-converged C_D values for the single-point and multipoint optimized aircraft at each design point. For the multipoint optimized CTW160, a 1.8% penalty is experienced at the nominal design point to achieve a 0.6% and 3.4% reduction in cruise C_D for the ±10% nominal C_L design points, respectively, and reductions of 13.7% and 12.7% in cruise C_D over the two high-speed design points. Meanwhile, for the multipoint optimized SBW160, C_D at the nominal operating condition is compromised by 2.6% to reduce C_D by 0.3% and 2.5% at design points 2 and 3, respectively, and around 10–11% at the two Mach 0.81 design points. These results illustrate that significant improvements to off-design performance can be achieved, especially at the high-speed design points, without severely degrading on-design performance. Compared to the multipoint optimized strut-braced-wing regional jet of

Chau and Zingg [36], however, a higher nominal performance penalty is observed for the multipoint optimized SBW160. This is likely due to the much higher nominal cruise C_L of the SBW160, i.e. 0.750 versus 0.682, which translates to more challenging off-design conditions.

Table 8 presents approximations of the full aircraft performance at each design point for each multipoint optimized design. These values are obtained by varying the payload of the nominal range mission within the conceptual design framework until the start of cruise C_L matches a given off-design C_L at the corresponding Mach number. The low-order contributions that result are then combined with the high-fidelity aerodynamic estimates to approximate the block fuel required for completing the nominal range mission at a given off-design condition. The relative block fuel performance of the multipoint optimized SBW160 is also provided in Figure 11, which indicates that the improvements to fuel efficiency are maintained across design points 2–5, further confirming the robustness of the design.

The optimized spanwise lift distributions for each optimized aircraft are shown in Figure 12. For the multipoint optimized CTW160, the spanwise lift distributions are similar between the single-point and multipoint optimized designs, except the latter features a more pronounced inboard wing loading, which is proportional to the increase in negative lift over the horizontal tail. For the SBW160, similar trends are seen to those of the single-point optimized SBW160. However, the optimizer has opted to further trade reduced inboard wing loading for more strut lift to accommodate the higher C_L requirement, while avoiding excessively high sectional lift coefficients over the wing.

Figure 13 shows the overall flow characteristics of the multipoint optimized CTW160 at the nominal design point, with those of the single-point optimized design included for reference. Shock surfaces are reintroduced over the upper wing surface of the multipoint optimized CTW160, as shown in Figure 13a, but are of very low strength. From Figure 13b, the isobars are still well-aligned with the sweep angle of the wing, albeit with some sudden changes in the surface pressure contours. These are caused by the necking of the pressure distributions shown in Figure 13c, which are incorporated to help improve off-design performance.

The overall flow characteristics of the single-point and multipoint optimized SBW160, evaluated at the nominal design point, are shown in Figure 14. As with the CTW160, the upper wing surface of the multipoint optimized SBW160 features relatively weak shocks, which can be seen in Figure 14a. The wing-strut junction, however, remains shock-free, even at each of the off-design conditions, although not shown here. From Figure 14b, the isobars of the multipoint optimized SBW160 also remain aligned with the geometric sweep of the wing, although some sudden changes in the surface pressure contours are again present. The weak shocks can be seen in the pressure distributions shown in Figure 14c, but the distributions remain relatively smooth. Of interest, however, is that the inboard sections of the strut, which carry more lift, are cambered, unlike those seen previously [35, 36], which were closer to symmetric in profile. This further supports the notion that there is some benefit to a lifting strut concept.

Examining the junction region of the wing and strut more closely through Figure 15, it can be seen that the absence of the adverse effects at the nominal design point leaves smooth surface pressure contours. Once again, the novel

Table 7 Optimized single-aisle aircraft performance at the nominal design point.

	Single-Point Optimum			*Multipoint Optimum*		
Parameter	CTW160	SBW160	Δ	CTW160	SBW160	Δ
			High Fidelity[1]			
L/D	21.71	24.00	+10.6%	21.32	23.39	+9.7%
C_L	0.524	0.750	+43.1%	0.524	0.750	+43.1%
C_D	0.0241	0.0312	+29.4%	0.0246	0.0321	+30.4%
Lift [lb]	148,040	144,770	−2.2%	148,040	144,770	−2.2%
Drag [lb]	6,820	6,030	−11.5%	6,940	6,190	−10.9%
			Low and High Fidelity[2]			
L/D	18.66	21.09	+13.0%	18.37	20.60	+12.2%
C_L	0.524	0.750	+43.1%	0.524	0.750	+43.1%
C_D	0.0281	0.0356	+26.6%	0.0285	0.0364	+27.6%
Lift [lb]	148,040	144,770	−2.2%	148,040	144,770	−2.2%
Drag [lb]	7,930	6,870	−13.5%	8,060	7,030	−12.8%
Block fuel [lb]	11,490	10,550	−8.2%	11,620	10,710	−7.8%

[1]Includes wing (and strut), fuselage, and horizontal tail contributions.

[2]Includes a 5% excrescence drag markup, and profile drag contributions from the vertical tail, nacelles, and pylons.

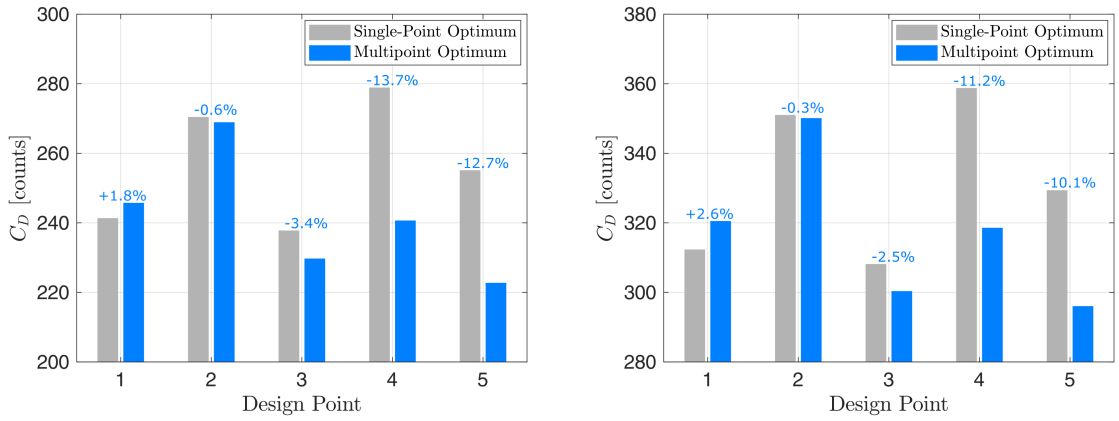

(a) CTW160 **(b) SBW160**

Fig. 10 Cruise drag performance at each design point of the five-point operating envelope.

Table 8 Multipoint optimized aircraft performance at the on- and off-design operating conditions.

Design Point	MP1	MP2	MP3	MP4	MP5
			CTW160		
L/D	18.37	18.69	17.51	16.68	15.83
C_L	0.524	0.576	0.472	0.472	0.419
C_D	0.0285	0.0308	0.0269	0.0283	0.0265
Lift [lb]	148,040	162,840	133,230	133,230	118,430
Drag [lb]	8,060	8,710	7,610	7,990	7,480
Block fuel [lb]	11,620	12,610	10,820	12,080	11,130
			SBW160		
L/D	20.60	20.96	19.63	18.51	17.53
C_L	0.750	0.825	0.675	0.675	0.600
C_D	0.0364	0.0393	0.0344	0.0365	0.0342
Lift [lb]	144,770	159,250	130,290	130,290	115,820
Drag [lb]	7,030	7,600	6,640	7,040	6,610
Block fuel [lb]	10,710	11,660	9,950	11,170	10,280

airfoil shapes featured around the wing-strut junction, along with the outwards force distribution, are present for both single-point and multipoint optimized designs, suggesting that they are generally favorable, and not necessarily an outcome of an optimizer exploitation that only amounts to small gains in performance.

VII. Mach Number and Lift Coefficient Sensitivity Studies

In order to further investigate the robustness of the multipoint optimized designs, the aerodynamic performance of each aircraft concept is examined in the regions around the Mach-C_L operating envelope bounded by the five design points of the multipoint optimizations. The first objective is to investigate the optimization robustness of each design by assessing the presence of point-optimization effects. This is achieved through a sweep of cruise C_L values ranging from -10% to $+10\%$ nominal C_L at the nominal Mach number for each aircraft, which is bounded by design points 2 and 3, and a sweep of cruise Mach numbers ranging from -0.03 to $+0.03$ nominal Mach at the nominal C_L, which extends beyond the envelope of design points. Cruise drag is evaluated at each operating point by trimming C_L with respect to the angle of attack at a given Mach number. These sensitivity studies are performed on the L0 grid level for reasons of computational cost.

Figures 16 and 17 show the results of the C_L sweep studies. Here, it can be seen that cruise C_D varies smoothly between design points 1, 2, and 3, with no indications that point-optimized features are present. Smooth drag rise behavior can also be seen in Figure 18 for both aircraft configurations. This suggests that the discrete multipoint objective function is sufficient for achieving a relatively robust design.

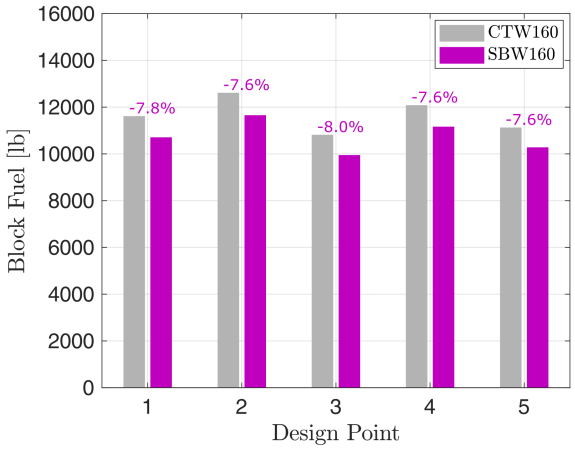

Fig. 11 Multipoint optimized block fuel burn comparisons at on- and off-design operating conditions.

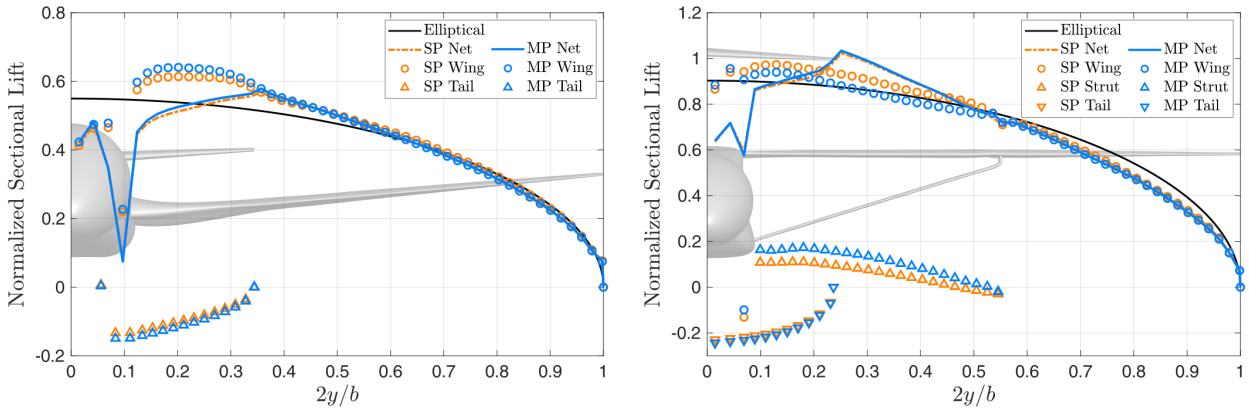

(a) CTW160 **(b) SBW160**

Fig. 12 Single-point and multipoint optimized spanwise lift distributions computed on the L0 grid level at the nominal design points.

The next objective is to examine the performance robustness of each aircraft concept from an aircraft design perspective. Since trends and tradeoffs can be expected to change from one grid level to another, the data points from the coarser L0 grid level are supplemented by several more refined data points obtained from Richardson extrapolation, namely, the theoretical L∞ values. These data points are included in Figures 16, 17, and 18, and indicate that the relative error associated with the optimization level grids are generally consistent, similar to the results of the grid convergence studies presented in Section VI. This suggests that trends and tradeoffs based on the L0 grid level can be expected to remain relatively constant as the grids are refined.

From Figure 17, the first observation is that the optimum C_L for maximum L/D at the design Mach number and cruise altitude is relatively close to the design C_L of each aircraft concept. The optimum values are approximately $C_L = 0.562$ and $C_L = 0.792$ for the multipoint optimized CTW160 and SBW160, respectively, which are higher than those of the nominal design points. This is expected, given that the design C_L of each aircraft concept corresponds to

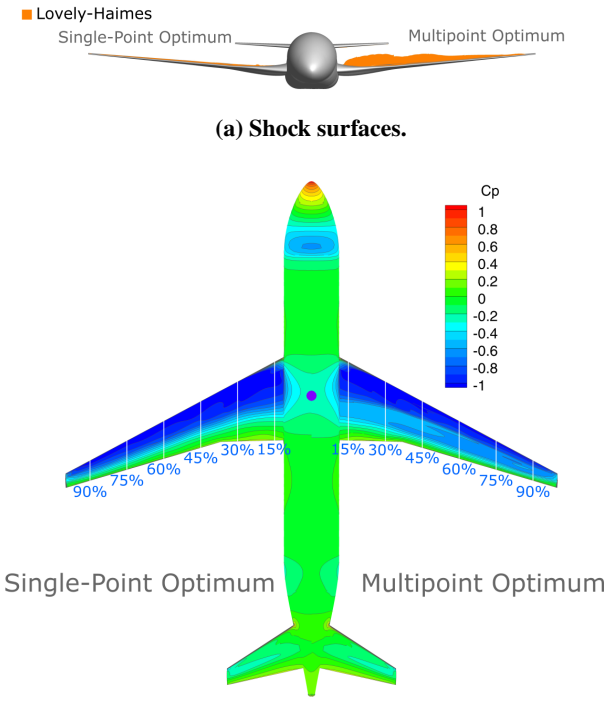

(a) Shock surfaces.

(b) Surface pressure contours and CG (purple circle).

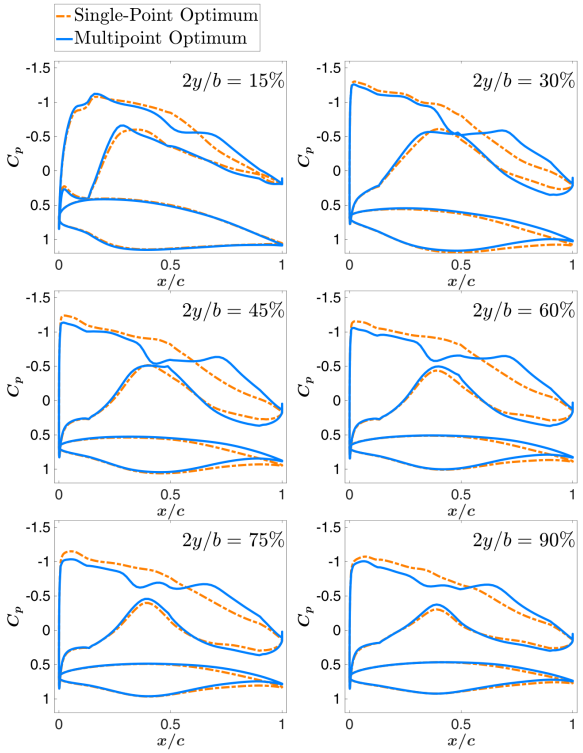

(c) Airfoil profiles and pressure distributions.

Fig. 13 CTW160: Single-point and multipoint optimized design and flow features. Flow features are computed on the L0 grid level at the nominal design point: $M = 0.78$ and $C_L = 0.524$.

the optimum C_L for minimum block fuel, which must trade favorably between operating at higher cruise altitudes at a given Mach number and wing loading, and increased climb and descent fuel.

The second observation is that the drag divergence Mach number is similar between each multipoint optimized aircraft, as shown in Figure 18. Assuming that drag divergence corresponds to $\mathrm{d}C_D/\mathrm{d}M = 0.10$ [51], the drag divergence Mach numbers are approximately $M = 0.803$ and $M = 0.796$ for the multipoint optimized CTW160 and SBW160, respectively. The reduced margin of the multipoint optimized SBW160 can be attributed to its much higher design C_L, although the difference is relatively small. Such an outcome is expected, suggesting that the improvements in fuel efficiency offered by transonic strut-braced-wing aircraft come at the cost of a slightly reduced operating envelope, given their more demanding optimum cruise lift coefficients. Nonetheless, it should be noted that for both aircraft, a delay in drag divergence can be achieved by considering a multipoint optimization formulation with a wider operating envelope. Depending on the width of such an envelope and the design weights placed on the operating conditions on its boundaries, however, this can incur increased nominal performance penalties. Alternatively, aircraft have the option of operating at lower cruise C_L values when cruising at higher Mach numbers, which typically shifts the drag rise curve down and to the right (see for example Kenway and Martins [52]).

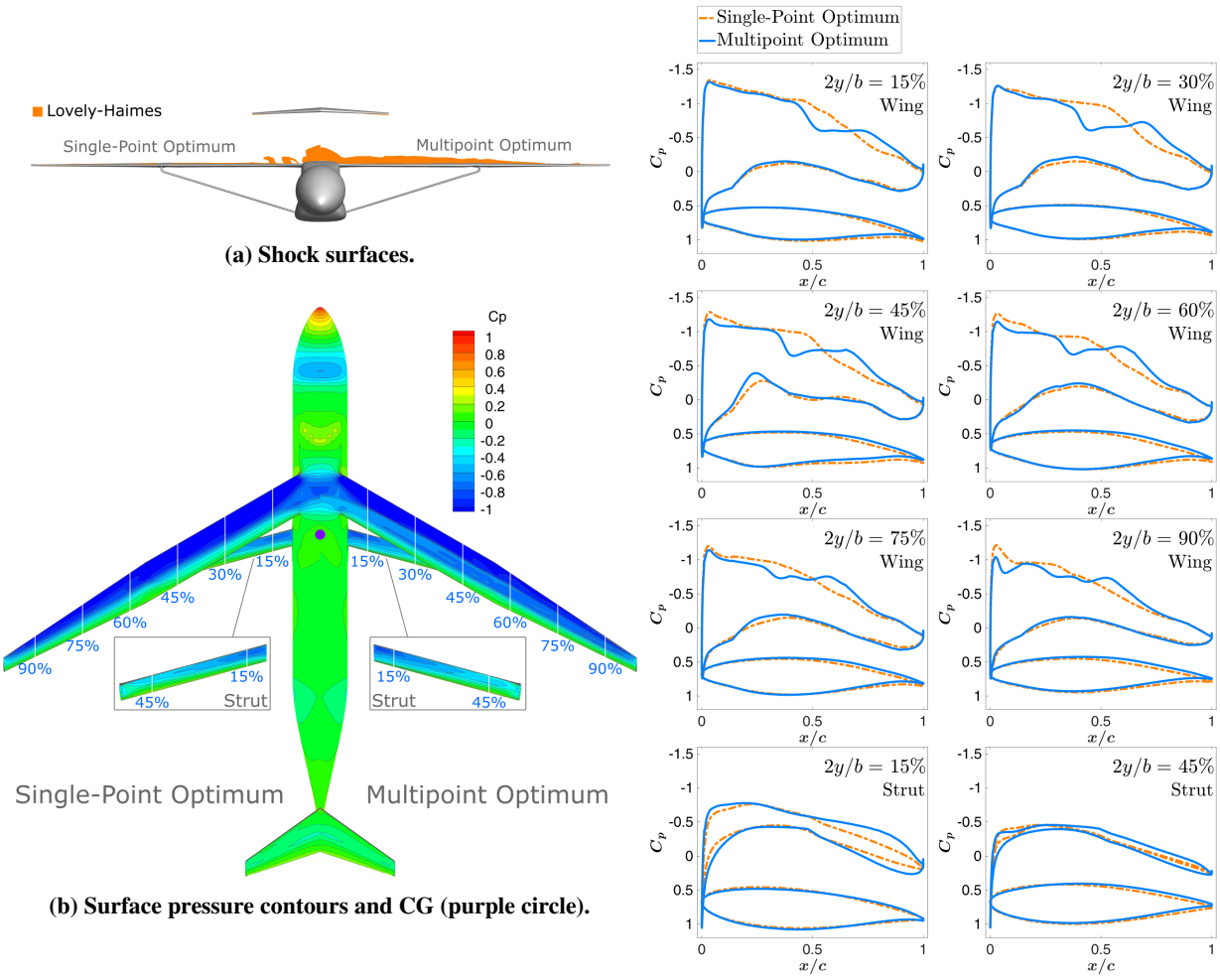

(a) Shock surfaces.

(b) Surface pressure contours and CG (purple circle).

(c) Airfoil profiles and pressure distributions.

Fig. 14 SBW160: Single-point and multipoint optimized design and flow features. Flow features are computed on the L0 grid level at the nominal design point: $M = 0.78$ and $C_L = 0.750$.

VIII. Conclusions

Through aerodynamic shape optimization based on the RANS equations, this work presents a highly credible assessment of the potential fuel burn benefits of a strut-braced-wing single-aisle aircraft. While comparable studies exist for the regional jet class, and assessments for single-aisle aircraft based on lower-fidelity models have been presented, to the authors' knowledge, the present paper represents the first published study investigating the transonic strut-braced-wing configuration in the single-aisle class using RANS-based aerodynamic shape optimization. Current technology levels are assumed and the performance benefits are measured relative to a similarly optimized conventional tube-and-wing representing the Airbus A320neo. Through single-point optimization, an aerodynamically efficient strut-braced wing design was achieved at Mach 0.78 and a design lift coefficient of 0.750, with the junction of the wing and strut free of shock formation and other adverse effects. The resulting aircraft design was found to provide a 13.5%

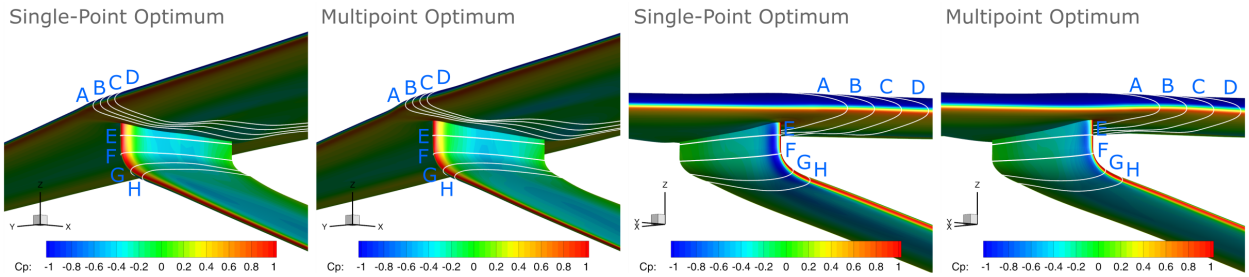

(a) Surface pressure contours.

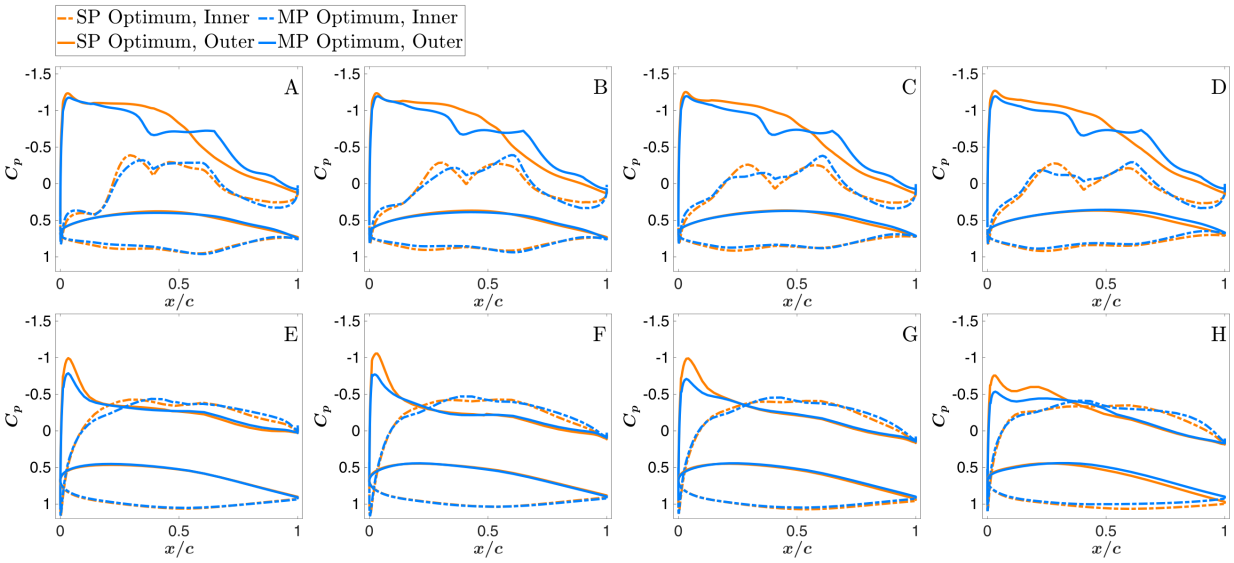

(b) Airfoil profiles and pressure distributions.

Fig. 15 SBW160: Single-point and multipoint optimized surface pressure contours with inner [(a),left] and outer [(a),right] views of the strut, and pressure distributions at different stations along the wing and strut. Results are computed on the L0 grid level at the nominal design point: $M = 0.78$ and $C_L = 0.750$.

reduction in cruise drag relative to the conventional tube-and-wing, which translates to an 8.2% savings in block fuel over a 1,000 nmi nominal mission.

Multipoint optimization further demonstrates that even with an operating envelope that includes design points expected to be more challenging for the strut-braced wing, namely, those at even higher Mach numbers and lift coefficients, on-design cruise drag is only compromised by 2.6% to reduce off-design cruise drag by up to 10–11%. The nominal mission block fuel savings reduces to 7.8% due to challenges associated with the relatively high design lift coefficient, but off-design block fuel savings remain significant at 7.6–8.0%.

Compared to the strut-braced-wing regional jet aircraft presented in References [35, 36], the strut-braced-wing single-aisle aircraft achieves a similar relative block fuel burn benefit, despite the advantage of its longer range nominal mission. The strut-braced-wing single-aisle aircraft also achieves its design lift coefficient at 42,220 ft due to its higher wing loading, reduced from the 44,670 ft of the regional jet class [35]. This suggests a decrease in both climb range

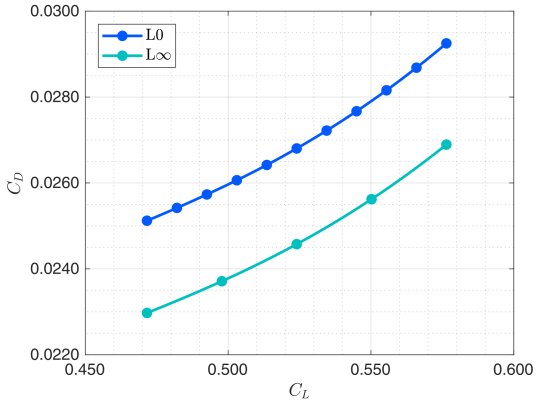

(a) CTW160 multipoint optimum.

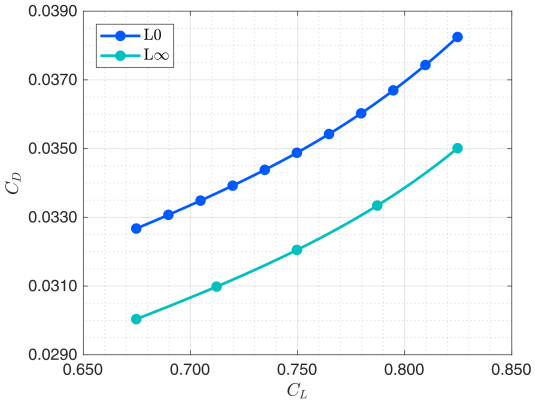

(b) SBW160 multipoint optimum.

Fig. 16 Drag polars at the nominal Mach numbers, initial cruise altitudes, and Reynolds numbers.

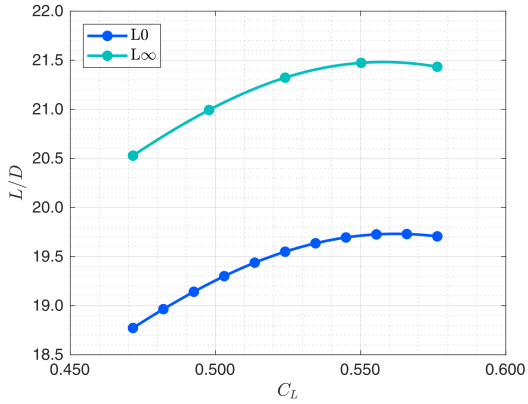

(a) CTW160 multipoint optimum.

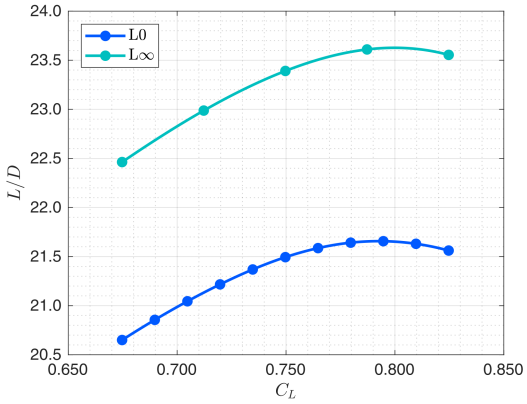

(b) SBW160 multipoint optimum.

Fig. 17 Aerodynamic efficiency at the nominal Mach numbers, initial cruise altitudes, and Reynolds numbers.

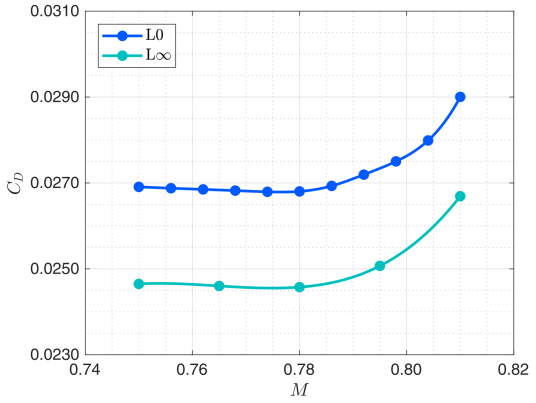

(a) CTW160 multipoint optimum.

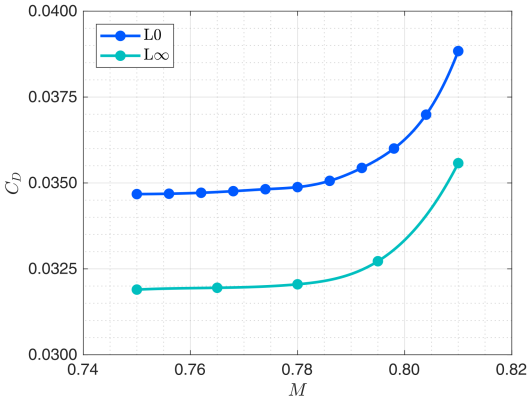

(b) SBW160 multipoint optimum.

Fig. 18 Drag rise performance at the nominal lift coefficients, initial cruise altitudes, and Reynolds numbers.

and fuel. However, operating at a higher cruise lift coefficient, while at Mach 0.78, appears to reduce its aerodynamic advantage over the Airbus A320neo-like conventional tube-and-wing aircraft. Indeed, results from the multipoint optimizations show that the penalty to on-design fuel burn performance is greater than that of the regional jet class due to the overall higher cruise lift coefficients considered when the same perturbations from the nominal design point are applied.

From the Mach number and lift coefficient sensitivity studies, the multipoint optimized strut-braced-wing aircraft was also shown to be relatively robust, with the design space remaining smooth about the nominal design point. Results indicate that the design cruise lift coefficient is relatively close to that of the optimal aerodynamic efficiency point but is reduced to accommodate trades with other disciplines and contributions to fuel burn, such as climb and descent. The multipoint optimized design also maintains a reasonable margin to drag divergence at the design cruise lift coefficient.

These results demonstrate the viability of the transonic strut-braced-wing configuration for the single-aisle class of transport aircraft, and the potential of the configuration for reducing commercial fleet fuel burn. This work also demonstrates the value of introducing high-fidelity aerodynamic shape optimization early in the preliminary design stage when investigating the benefits of novel aircraft configurations that experience unconventional flow features and adverse effects, which go beyond the capabilities of lower order models often employed in conceptual aircraft design.

Acknowledgments

Financial support is provided in part by the Natural Sciences and Engineering Research Council of Canada, the Queen Elizabeth II Graduate Scholarship in Science and Technology, the Ontario Graduate Scholarship, and the University of Toronto. Computations were performed on the Niagara supercomputer at the SciNet HPC Consortium. SciNet is funded by the Canada Foundation for Innovation under the auspices of Compute Canada; the Government of Ontario; the Ontario Research Fund - Research Excellence; and the University of Toronto.

References

[1] Bravo-Mosquera, P. D., Catalano, F. M., and Zingg, D. W., "Unconventional Aircraft for Civil Aviation: A Review of Concepts and Design Methodologies," *Progress in Aerospace Sciences*, Vol. 131, 2022. https://doi.org/10.1016/j.paerosci.2022.100813, article 100813.

[2] Liebeck, R. H., "Design of the Blended Wing Body Subsonic Transport," *Journal of Aircraft*, Vol. 41, No. 1, 2004, pp. 10–25. https://doi.org/10.2514/1.9084.

[3] Reist, T. A., and Zingg, D. W., "High-Fidelity Aerodynamic Shape Optimization of a Lifting-Fuselage Concept for Regional Aircraft," *Journal of Aircraft*, Vol. 54, No. 3, 2017, pp. 1085–1097. https://doi.org/10.2514/1.C033798.

[4] Wolkovitch, J., "The Joined Wing: An Overview," *Journal of Aircraft*, Vol. 23, No. 3, 1986, pp. 161–178. https://doi.org/10.2514/3.45285.

[5] Prandtl, L., "Induced Drag of Multiplanes," Tech. rep., NACA, March 1924. TN-182.

[6] Frediani, A., "The Prandtl Wing," *Innovative Configurations and Advanced Concepts for Future Civil Transport Aircraft*, edited by E. Torenbeek and H. Deconinck, von Karman Institute for Fluid Dynamics, 2005. VKI Lecture Series.

[7] Cavallaro, R., and Demasi, L., "Challenges, Ideas, and Innovations of Joined-Wing Configurations: A Concept from the Past, an Opportunity for the Future," *Progress in Aerospace Sciences*, Vol. 87, 2016, pp. 1–93. https://doi.org/10.1016/j.paerosci.2016.07.002.

[8] Drela, M., "Development of the D8 Transport Configuration," *29th AIAA Applied Aerodynamics Conference*, AIAA 2011-3970, Honolulu, Hawaii, June 2011. https://doi.org/10.2514/6.2011-3970.

[9] Benad, J., "The Flying V A New Aircraft Configuration for Commercial Passenger Transport," *Deutscher Luft- und Raumfahrtkongress*, Duetsche Gesellschaft für Luft- und Raumfahrt, Rostock, Mecklenburg-Vorpommern, September 2015. https://doi.org/10.25967/370094.

[10] Welstead, J. R., and Felder, J. L., "Conceptual Design of a Single-Aisle Turboelectric Commercial Transport with Fuselage Boundary Layer Ingestion," *54th AIAA Aerospace Sciences Meeting*, AIAA 2016-1027, San Diego, CA, January 2016. https://doi.org/10.2514/6.2016-1027.

[11] Chau, T., Kenway, G. K. W., and Kiris, C., "Conceptual Exploration of Aircraft Configurations for the SUSAN Electrofan," *AIAA SciTech Forum and Exposition*, AIAA 2022-2181, San Diego, CA, January 2022. https://doi.org/10.2514/6.2022-2181.

[12] Bradley, M. K., and Droney, C. K., "Subsonic Ultra Green Aircraft Research: Phase II - Volume II - Hybrid Electric Design Exploration," Tech. rep., Boeing Research and Technology, April 2015. NASA/CR-2015-218704/Volume II.

[13] Schmollgruber, P., Donjat, D., Ridel, M., Cafarelli, I., Atinault, O., François, C., and Paluch, B., "Multidisciplinary Design and Performance of the ONERA Hybrid Electric Distributed Propulsion Concept (DRAGON)," *AIAA SciTech Forum and Exposition*, AIAA 2020-0501, Orlando, FL, January 2020. https://doi.org/10.2514/6.2020-0501.

[14] Pfenninger, W., "Design Considerations of Large Subsonic Long Range Transport Airplanes with Low Drag Boundary Layer Suction," Tech. rep., Northrop Aircraft Incorporated, November 1954. NAI-54-800 (BLC-67).

[15] Grasmeyer, J. M., Naghshineh, A., Tetrault, P. A., Grossman, B., Haftka, R. T., Kapania, R. K., Mason, W. H., and Schetz, J. A., "Multidisciplinary Design Optimization of a Strut-Braced Wing Aircraft with Tip-Mounted Engines," Tech. rep., NASA Langley Research Center, January 1998. MAD 98-01-01.

[16] Gern, F. H., Ko, A., Sulaeman, E., Gundlach, J. F., Kapania, R. K., and Haftka, R. T., "Multidisciplinary Design Optimization of a Transonic Commercial Transport with Strut-Braced Wing," *Journal of Aircraft*, Vol. 38, No. 6, 2001, pp. 1006–1014. https://doi.org/10.2514/2.2887.

[17] Gur, O., Bhatia, M., Schetz, J. A., Mason, W. H., Kapania, R. K., and Mavris, D. N., "Design Optimization of a Truss-Braced-Wing Transonic Transport Aircraft," *Journal of Aircraft*, Vol. 47, No. 6, 2010, pp. 1907–1917. https://doi.org/10.2514/1.47546.

[18] Meadows, N. A., Schetz, J. A., Kapania, R. K., Bhatia, M., and Seber, G., "Multidisciplinary Design Optimization of Medium-Range Transonic Truss-Braced Wing Transport Aircraft," *Journal of Aircraft*, Vol. 49, No. 6, 2012, pp. 1006–1014. https://doi.org/10.2514/1.C031695.

[19] Chakraborty, I., Nam, T., Gross, J. R., Mavris, D. N., Schetz, J. A., and Kapania, R. K., "Comparative Assessment of Strut-Braced and Truss-Braced Wing Configurations Using Multidisciplinary Design Optimization," *Journal of Aircraft*, Vol. 52, No. 6, 2015, pp. 2009–2020. https://doi.org/10.2514/1.C033120.

[20] Bartels, R. E., Scott, R. C., Allen, T. J., and Sexton, B. W., "Aeroelastic Analysis of SUGAR Truss-Braced Wing Wind-Tunnel Model Using FUN3D and a Nonlinear Structural Model," *AIAA Scitech Forum*, AIAA 2015-1174, Kissimmee, FL, January 2015. https://doi.org/10.2514/6.2015-1174.

[21] Bartels, R. E., Funk, C. J., and Scott, R. C., "Limit-Cycle Oscillation of the Subsonic Ultra-Green Aircraft Research Truss-Braced Wing Aeroelastic Model," *Journal of Aircraft*, Vol. 54, No. 5, 2017, pp. 1605–1612. https://doi.org/10.2514/1.C034064.

[22] Mallik, W., Kapania, R. K., and Schetz, J. A., "Effect of Flutter on the Multidisciplinary Design Optimization of Truss-Braced-Wing Aircraft," *Journal of Aircraft*, Vol. 52, No. 6, 2015, pp. 1858–1872. https://doi.org/10.2514/1.C033096.

[23] Sohst, M., Lobo do Vale, J., Afonso, F., and Suleman, A., "Optimization and Comparison of Strut-Braced and High Aspect Ratio Wing Aircraft Configurations Including Flutter Analysis with Geometric Non-Linearities," *Aerospace Science and Technology*, 2022. https://doi.org/10.1016/j.ast.2022.107531, in press.

[24] Ma, Y., Karpuk, S., and Elham, A., "Conceptual Design and Comparative Study of Strut-Braced Wing and Twin-Fuselage Aircraft Configurations with Ultra-High Aspect Ratio Wings," *Aerospace Science and Technology*, Vol. 121, 2022. https://doi.org/10.1016/j.ast.2022.107395, article 107395.

[25] Bieler, H., Bier, N., Bugeda, G., Periaux, J., Redondo, D., Guttila, S., and Pons, J., "A Common Platform for Validation of Aircraft Drag Reduction Technologies," retrieved on 1 May 2018. URL http://congress.cimne.com/padri-2017/frontal/default.asp.

[26] Kenway, G., Housman, J., and Kiris, C., "NASA Ames Research Center Contributions to the PADRI Workshop," *Platform for Aircraft Drag Reduction Innovation*, ECCOMAS, Barcelona, Spain, November 2017.

[27] Secco, N. R., and Martins, J. R. R. A., "RANS-Based Aerodynamic Shape Optimization of a Strut-Braced Wing with Overset Meshes," *Journal of Aircraft*, Vol. 56, No. 1, 2019, pp. 217–227. https://doi.org/10.2514/1.C034934.

[28] Li, L., Bai, J., and Qu, F., "Multipoint Aerodynamic Shape Optimization of a Truss-Braced-Wing Aircraft," *Journal of Aircraft*, 2022. https://doi.org/10.2514/1.C036413, in press.

[29] Wood, N., "Strut Braced Wings, a Challenge or an Opportunity?" retrieved on 1 May 2018. URL http://congress.cimne.com/padri-2017/frontal/default.asp.

[30] Bradley, M. K., Droney, C. K., and Allen, T. J., "Subsonic Ultra Green Aircraft Research: Phase II - Volume I - Truss Braced Wing Design Exploration," Tech. rep., Boeing Research and Technology, April 2015. NASA/CR-2015-218704/Volume I.

[31] Harrison, N. A., Beyar, M. D., Dickey, E. D., Hoffman, K., Gatlin, G. M., and Viken, S. A., "Development of an Efficient Mach = 0.80 Transonic Truss-Braced Wing Aircraft," *AIAA Scitech Forum*, AIAA 2020-0011, Orlando, Florida, January 2020. https://doi.org/10.2514/6.2020-0011.

[32] Maldonado, D., Housman, J. A., Piotrowski, M. G. H., Kiris, C. C., Hunter, C. A., Viken, S. A., McMillin, S. N., and Milholen, W. E., "Improvements in Simulating a Mach 0.80 Transonic Truss-Braced Wing Configuration using the Spalart-Allmaras and k-omega SST Turbulence Models," *AIAA Scitech Forum*, AIAA 2021-1531, Virtual Event, January 2021. https://doi.org/10.2514/6.2021-1531.

[33] Carrier, G., Arnoult, G., Fabbiane, N., Schotté, J.-S., David, C., Defoort, S., Delavenne, M., and Bénard, E., "Multidisciplinary Analysis and Design of Strut-Braced Wing Concept for Medium Range Aircraft," *AIAA SciTech Forum and Exposition*, AIAA 2022-0726, San Diego, CA, January 2022.

[34] Gagnon, H., and Zingg, D. W., "Aerodynamic Trade Study of a Box-Wing Aircraft Configuration," *Journal of Aircraft*, Vol. 53, No. 4, 2016, pp. 971–981. https://doi.org/10.2514/1.C033592.

[35] Chau, T., and Zingg, D. W., "Aerodynamic Design Optimization of a Transonic Strut-Braced-Wing Regional Aircraft," *Journal of Aircraft*, Vol. 59, No. 1, 2022, pp. 253–271. https://doi.org/10.2514/1.C036389.

[36] Chau, T., and Zingg, D. W., "Fuel Burn Evaluation of a Transonic Strut-Braced-Wing Regional Aircraft through Multipoint Aerodynamic Optimization," *The Aeronautical Journal*, 2022. In press.

[37] Turriziani, R. Y., Lovell, W. A., Martin, G. L., Price, J. E., Swanson, E. E., and Washburn, G. F., "Preliminary Design Characteristics of a Subsonic Business Jet Concept Employing an Aspect Ratio 25 Strut-Braced Wing," Tech. rep., NASA, October 1980. NASA-CR-159361.

[38] "FAA Aerospace Forecast - Fiscal Years 2019-2039," Federal Aviation Administration, retrieved on 20 October 2020. URL https://www.faa.gov/data_research/aviation/aerospace_forecasts/.

[39] "Global Market Forecast - Cities, Airports & Aircraft 2019-2038," Airbus, retrieved on 20 October 2020. URL https://gmf.airbus.com.

[40] Maldonado, D., Housman, J. A., Duensing, J. C., Jensen, J. C., Kiris, C. C., Viken, S. A., Hunter, C. A., Frink, N. T., and McMillin, S. N., "Computational Simulations of a Mach 0.745 Transonic Truss-Braced Wing Design," *AIAA Scitech Forum*, AIAA 2020-1649, Orlando, Florida, January 2020. https://doi.org/10.2514/6.2020-1649.

[41] NASA, "Sustainable Flight Demonstrator Project," retrieved on 4 February 2023. URL https://www.nasa.gov/aeroresearch/programs/iasp/sfd/description/.

[42] Carrier, G., Atinault, O., Dequand, S., Hantrais-Gervois, J.-L., Liauzun, C., Paluch, B., Rodde, A.-M., and Toussaint, C., "Investigation of a Strut-Braced Wing Configuration for Future Commercial Transport," *28th International Congress of the Aeronautical Sciences*, ICAS 2012-1.10.2, Brisbane, Australia, September 2012.

[43] Moerland, E., Pfeiffer, T., Böhnke, D., Jepsen, J., Freund, S., Liersch, C. M., Chiozzotto, G. P., Klein, C., Scherer, J., Hasan, Y. J., and Flink, J., "On the Design of a Strut-Braced Wing Configuration in a Collaborative Design Environment," *AIAA Aviation Forum*, AIAA 2017-4397, Denver, Colorado, June 2017. https://doi.org/10.2514/6.2017-4397.

[44] Zingg, D. W., Chau, T., Gray, A. L., and Reist, T. A., "A Multifidelity Multidisciplinary Approach to Unconventional Aircraft Development and Assessment with Application to the Strut-Braced Wing and Hybrid Wing-Body Configurations," *33rd Congress of the International Council of the Aeronautical Sciences*, Stockholm, Sweden, September 2022.

[45] Airbus Canada Limited Partnership, *A220-300 Airport Planning Publication APP*, 2020. Issue 22 - 17 September 2020.

[46] Osusky, L., Buckley, H. P., Reist, T. A., and Zingg, D. W., "Drag Minimization Based on the Navier-Stokes Equations Using a Newton-Krylov Approach," *AIAA Journal*, Vol. 53, No. 6, 2015, pp. 1555–1577. https://doi.org/10.2514/1.J053457.

[47] Vassberg, J. C., Tinoco, E. N., Mani, M., Rider, B., Zickuhr, T., Levy, D. W., Brodersen, O. P., Eisfeld, B., Crippa, S., Wahls, R. A., Morrison, J. H., Mavriplis, D. J., and Murayama, M., "Summary of the Fourth AIAA Computational Fluid Dynamics Drag Prediction Workshop," *Journal of Aircraft*, Vol. 51, No. 4, 2014, pp. 1070–1089. https://doi.org/10.2514/1.C032418.

[48] Roache, P. J., *Verification and Validation in Computational Science and Engineering*, 1st ed., Hermosa Publishers, 1998. Albuquerque, NM,.

[49] Gagnon, H., and Zingg, D. W., "Euler-Equation-Based Drag Minimization of Unconventional Aircraft," *Journal of Aircraft*, Vol. 53, No. 5, 2016, pp. 1361–1371. https://doi.org/10.2514/1.C033591.

[50] Demasi, L., Monegato, G., Cavallaro, R., and Rybarczyk, R., "Minimum Induced Drag Conditions for Truss-Braced Wings," *AIAA Journal*, Vol. 56, No. 12, 2018, pp. 4669–4684. https://doi.org/10.2514/1.J057225.

[51] Malone, B., and Mason, W. H., "Multidisciplinary Optimization in Aircraft Design Using Analytic Technology Models," *Journal of Aircraft*, Vol. 32, No. 2, 1995, pp. 431–438. https://doi.org/10.2514/3.46734.

[52] Kenway, G. K. W., and Martins, J. R. R. A., "Multipoint Aerodynamic Shape Optimization Investigations of the Common Research Model Wing," *AIAA Journal*, Vol. 54, No. 1, 2016, pp. 113–128. https://doi.org/10.2514/1.J054154.

[53] Raymer, D. P., *Aircraft Design: A Conceptual Approach*, 5th ed., American Institute of Aeronautics and Astronautics, 2012.

[54] Torenbeek, E., *Synthesis of Subsonic Airplane Design*, Delft University, 1982.

[55] Kroo, I., and Shevell, R., "Aircraft Design, Synthesis and Analysis," retrieved on 23 December 2016. URL http://adg.stanford.edu/aa241/AircraftDesign.html.

[56] Andrews, S. A., Perez, R. E., and Wowk, D., "Wing Weight Model for Conceptual Design of Nonplanar Configurations," *Aerospace Science and Technology*, Vol. 43, No. 1, 2015, pp. 51–62. https://doi.org/10.1016/J.AST.2015.02.011.

[57] Torenbeek, E., "Development and Application of a Comprehensive, Design-Sensitive Weight Prediction Method for Wing Structures of Transport Category Aircraft," Tech. rep., Delft University of Technology, September 1992. LR-693.

[58] Gur, O., Bhatia, M., Mason, W. H., Schetz, J. A., Kapania, R. K., and Nam, T., "Development of Framework for Truss-Braced Wing Conceptual MDO," *51st AIAA Structures, Structural Dynamics, and Materials Conference*, AIAA 2010-2754, Orlando, Florida, April 2010. https://doi.org/10.2514/6.2010-2754.

[59] Williams, J. E., and Vukelich, S. R., "The USAF Stability and Control Digital DATCOM - Volume II - Implementation of Datcom Methods," Tech. rep., McDonnell Douglas Astronautics Company, April 1979. AFFDL-TR-79-3032.

[60] Hicken, J. E., and Zingg, D. W., "Aerodynamic Optimization Algorithm with Integrated Geometry Parameterization and Mesh Movement," *AIAA Journal*, Vol. 48, No. 2, 2010, pp. 400–413. https://doi.org/10.2514/1.44033.

[61] Gagnon, H., and Zingg, D. W., "Two-Level Free-Form and Axial Deformation for Exploratory Aerodynamic Shape Optimization," *AIAA Journal*, Vol. 53, No. 7, 2015, pp. 2015–2026. https://doi.org/10.2514/1.J053575.

[62] Sederberg, T. W., and Parry, S. R., "Free-Form Deformation of Solid Geometric Models," *ACM SIGGRAPH Computer Graphics*, Vol. 20, No. 4, 1986, pp. 151–160. https://doi.org/10.1145/15886.15903.

[63] Osusky, M., and Zingg, D. W., "Parallel Newton-Krylov-Schur Solver for the Navier-Stokes Equations Discretized Using Summation-By-Parts Operators," *AIAA Journal*, Vol. 51, No. 12, 2013, pp. 2833–2851. https://doi.org/10.2514/1.J052487.

[64] Allmaras, S. R., Johnson, F. T., and Spalart, P. R., "Modifications and Clarifications for the Implementation of the Spalart-Allmaras Turbulence Model," *7th International Conference on Computational Fluid Dynamics*, ICCFD7-1902, Big Island, Hawaii, July 2012.

[65] Spalart, P. R., "Strategies for Turbulence Modelling and Simulations," *International Journal of Heat and Fluid Flow*, Vol. 21, No. 3, 2000, pp. 252–263. https://doi.org/10.1016/S0142-727X(00)00007-2.

[66] Gill, P. E., Murray, W., and Saunders, M. A., "SNOPT: An SQP Algorithm for Large-Scale Constrained Optimization," *SIAM Journal on Optimization*, Vol. 14, No. 4, 2002, pp. 979–1006. https://doi.org/10.1137/S0036144504446096.

[67] Pironneau, O., "On Optimum Design in Fluid Mechanics," *Journal of Fluid Mechanics*, Vol. 64, No. 1, 1974, pp. 97–110. https://doi.org/10.1017/S0022112074002023.

[68] Jameson, A., "Aerodynamic Design via Control Theory," *Journal of Scientific Computing*, Vol. 3, No. 3, 1998, pp. 223–260. https://doi.org/10.1007/BF01061285.

[69] Squire, W., and Trapp, G., "Using Complex Variables to Estimate Derivatives of Real Functions," *SIAM Review*, Vol. 40, No. 1, 1998, pp. 110–112. https://doi.org/10.1137/S003614459631241X.

[70] Cumpsty, N., Mavris, D., Alonso, J., Catalano, F., Eyers, C., Goutines, M., Grönstedt, T., Hileman, J., Joselzon, A., Khaletskii, I., Ogilvie, F., Ralph, M., Sabnis, J., Wahls, R., and Zingg, D., "Independent Expert Integrated Technology Goals Assessment and Review for Engines and Aircraft," Tech. rep., International Civil Aviation Organization, February 2019. CAEP/11-WP/24.

[71] "Type-Certificate Data Sheet for PW1100G-JM Series Engines," Tech. rep., European Union Aviation Safety Agency, December 2019. No. IM.E.093.

[72] Airbus S.A.S., *A320 Aircraft Characteristics - Airport and Maintanance Planning*, 2005. Revision 36 - 01 February 2019.

[73] Anderson, B. T., and Meyer, R. R., "Effects of Wing Sweep on In-Flight Boundary-Layer Transition for a Laminar Flow Wing at Mach Numbers From 0.60 to 0.79," Tech. rep., NASA, July 1990. NASA TM-101701.

[74] Gur, O., Mason, W. H., and Schetz, J. A., "Full-Configuration Drag Estimation," *Journal of Aircraft*, Vol. 47, No. 4, 2010, pp. 1356–1367. https://doi.org/10.2514/1.47557.

[75] Mason, W. H., "Analytic Models for Technology Integration in Aircraft Design," *Aircraft Design, Systems, and Operations Conference*, AIAA 90-3262, Dayton, OH, September 1990. https://doi.org/10.2514/6.1990-3262.

A. Conceptual Multidisciplinary Design Optimization Framework

This appendix provides an overview of Faber, a low-order MDO framework developed at the University of Toronto for the conceptual design of transport aircraft. The main components are disciplinary analysis modules for aerodynamics, weight and balance, structures, propulsion, and performance, which for a given aircraft concept and set of design missions, are used in an iterative routine to size the weights of the aircraft components and subsystems. In order to optimize the aircraft concept, this sizing routine is integrated within a gradient-based optimization framework, which provides the means for efficiently refining an initial concept for minimum fuel burn while subject to top level aircraft requirements in the form of linear and nonlinear constraints. A summary of each disciplinary analysis module is presented in the following sections, while more details can be found in Chau and Zingg [35].

A. Aerodynamics

The aerodynamics module approximates lift and drag assuming steady level flight at a given operating condition. With lift set equal to weight at cruise, cruise drag is approximated through low-order approximations for profile drag, induced drag, and wave drag. Profile drag is calculated through the component buildup method of Raymer [53], which includes contributions from skin friction drag, form drag, interference drag, and excrescence drag for wings, struts, fuselages, horizontal and vertical tails, nacelles, and pylons. Induced drag is calculated with a vortex lattice method coupled with a Trefftz-plane analysis, while wave drag is approximated via the Korn equation corrected for swept wings [51]. These drag contributions are assumed to only come from the wing, with spanwise lift distributions assumed to be elliptical. As an approximation, trim drag is considered negligible.

B. Weight and Balance

For conventional aircraft components and subsystems, weights are calculated with the empirical methods of Torenbeek [54]. This includes all contributions except for those of the wing. For the center of gravity (CG) locations, however, contributions from all aircraft components and subsystems are approximated with the statistical correlations of

Torenbeek [54], and Kroo and Shevell [55]. Fuel weights are calculated through the performance module, with the CG locations determined based on the volume centroid of the fuel tanks.

C. Structures

For estimating the weight of the wing, Faber employs a semi-empirical method that can capture the structural efficiency of unconventional wing systems such as the strut-braced wing. Primary or structural wing weights are computed using an equivalent beam model [56] in a finite-element method. Load conditions include $+2.5g$ and $-1g$ symmetric maneuvers, and structures are sized to be fully stressed. For secondary or non-structural wing weights, approximations are provided by the statistical correlations of Torenbeek [57]. These include wing ribs, minimum gauge structures (i.e. fixed leading and trailing edges), high-lift devices (i.e. slats, flaps, and spoilers), flight control systems (i.e. ailerons), support structures, and non-optimum structures, all assumed to be conventional. For wing spans that exceed a given gate limit, e.g. 118 ft for code C gates, a contribution to the secondary wing weights is included for a wing folding mechanism calculated using the method of Gur et al. [58]. A global buckling detection method is also included for strut-braced wings, which can accommodate columns with nonuniform stiffness distributions.

D. Propulsion

The propulsion module consists of sizing and analysis methods provided by Gur et al. [58], which includes scaling laws for resizing the dry weight, maximum length, and maximum diameter of a given reference engine based on a specified maximum thrust value. Statistical correlations are also provided for approximating the thrust specific fuel consumption (TSFC) and thrust available at a given Mach number and altitude as a function of the maximum thrust. Parametric models of the nacelles and pylons are also included, which allows them to be resized as the maximum thrust, and hence maximum length and diameter, of a given podded engine is modified.

E. Performance

The performance module calculates mission and block fuel through the method of fuel fractions, as shown in Figure 19. For takeoff (including warmup and taxi), climb, and landing, the following fuel fractions are used:

$$F_{\text{takeoff}} = 0.995 \tag{4}$$

$$F_{\text{climb}} = 1 - 0.013(\text{ICA}/30,000) \tag{5}$$

$$F_{\text{land}} = 0.998 \tag{6}$$

where ICA is the initial cruise altitude or the change in altitude associated with a step climb in feet. For missions with a range of 2,500 nmi or more, two cruise segments are assumed, separated by a step climb of 2,000 ft. Although already

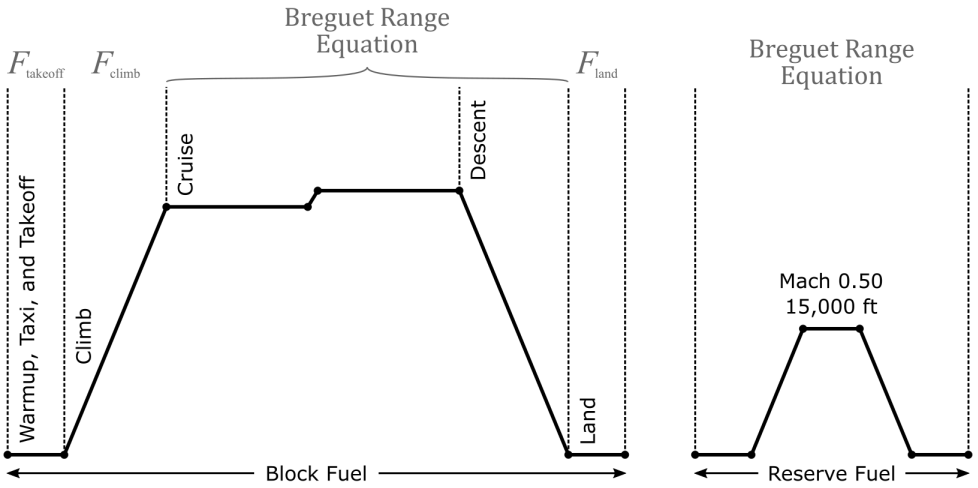

Fig. 19 Mission profile for fuel burn calculations.

accounted for in F_{takeoff}, the fuel required for warmup and taxi is calculated through $F_{\text{warmtaxi}} = 0.9954$ based on the Airbus A320neo. This fuel fraction is used to calculate the takeoff weight at the beginning of a given mission. For cruise, the fuel fraction is given by the Breguet range equation

$$F_{\text{cruise}} = \exp\left(-\frac{R \cdot \text{TSFC}}{aM(L/D)}\right) \tag{7}$$

where R is the cruise range, TSFC is the thrust specific fuel consumption, and a, M, and L/D are the speed of sound, Mach number, and lift-to-drag ratio, respectively.

In order to account for the range spent climbing, a notional climb profile is assumed with three climb segments: a climb at a calibrated airspeed (CAS) of 250 knots from 1,500 ft to 10,000 ft, an accelerated climb at 270 knots CAS until the cruise Mach number is achieved, and a constant Mach number climb to the initial cruise altitude.

As recommended by Torenbeek [54], a first-order approximation for the fuel burn of the descent segment can be obtained by treating it as an extended cruise segment. In particular, the fuel fraction for the descent segment, F_{descent}, is determined by the Breguet range equation, and a reduction in cruise range for the cruise segment calculation is not needed. Although generally conservative, this avoids making assumptions about the descent profile and idle thrust settings.

Once the fuel fractions have been determined, the total fuel burn for a given mission profile can then be computed through the products of each contribution:

$$W_{\text{fuel}} = \frac{1 - \Pi_i F_i}{\Pi_i F_i}(\text{OEW} + W_{\text{payload}}) \tag{8}$$

where i is the segment index.

Reserve fuel is also included for a 200 nmi diversion and a 45 minute hold. These requirements are converted into an equivalent range, and the reserve fuel is approximated through the Breguet range equation at a Mach number of 0.50 and an altitude of 15,000 ft.

F. Miscellaneous

Stability and buffet modules are also included, which provide additional metrics used to enforce optimization constraints. For stability, estimates of the static margin are included based on the DATCOM method [59] and approximations provided by Torenbeek [54]. For buffet, a heuristic is included based on a low-order analysis of a notional buffet envelope and assumes that buffet is preceded by strong shock formation as indicated by the Korn equation [51]. This buffet heuristic is used to prevent the design lift coefficients of strut-braced wings from becoming exceedingly high, which is often necessary for attaining more optimal lift-to-drag ratios [35, 37].

B. High-Fidelity Aerodynamic Shape Optimization Framework

This appendix presents an overview of Jetstream, a high-fidelity aerodynamic shape optimization framework that has also been developed at the University of Toronto. The main components include: (1) an integrated mesh parameterization and deformation scheme, (2) a free-form and axial deformation geometry control system, (3) a three-dimensional structured multiblock flow solver for the RANS equations, and (4) a gradient-based optimizer with gradient evaluation, which provide the means for automating the aerodynamic design of a given aircraft through accurate simulations of the flow physics.

A. Integrated Mesh Parameterization and Deformation

In order to update the computational grid as the aerodynamic surfaces are deformed, Jetstream includes an integrated mesh parameterization and deformation scheme [60]. Given a baseline structured multiblock mesh, a parametric model is created by parameterizing each block with B-spline volumes. As the B-spline control points defining the aerodynamic surfaces are deformed, changes are propagated in parallel across the control points of each B-spline volume through a robust linear elasticity model. The mesh parameterization is also used to generate additional grid levels for performing grid convergence studies. This is done through automatic grid node insertion and redistribution, which maintains the mesh spacing functions of the baseline grid [46].

B. Geometry Control

Geometry control is provided by the two-level deformation method of Gagnon and Zingg [61]. In this approach, the B-spline control points defining the aerodynamic surfaces are embedded within free-form deformation (FFD) volumes [62], which provide local or sectional shape control, and are driven by axial curves that provide global or planform shape control. The FFD volumes are B-spline volumes which consist of FFD-volume cross-sections distributed

in the spanwise direction, each with FFD-volume control point pairs distributed uniformly in the chordwise direction. Design variables are defined through transformation operators applied to the xyz-coordinates of the FFD-volume control points, which for a given FFD-volume cross-section are given by:

- **Twist:** a rotation of the FFD-volume cross-section in the local xz-plane about the local origin
- **Taper:** a uniform scaling of the FFD-volume cross-section in the local xz-plane with respect to the local origin
- **Section Shape:** a scaling of the vertical distance from the local origin to the position of a given FFD-volume control point along the local z-axis; this design variable is defined separately for each individual FFD-volume control point

The local coordinate system of each FFD-volume cross-section is defined by the position of an axial curve, which is threaded through each FFD-volume cross-section of a given FFD volume. These axial curves are B-spline curves that can be manipulated via axial curve control points to change the position and orientation of each FFD-volume cross-section. The planform design variables are defined as follows:

- **Sweep:** a translation in the x-coordinate of a given axial curve control point
- **Span:** a translation in the y-coordinate of a given axial curve control point
- **Dihedral:** a translation in the z-coordinate of a given axial curve control point

C. Flow Solver

For computing aerodynamic functionals such as lift and drag, a three-dimensional parallel implicit structured multiblock Newton-Krylov flow solver [63] is used to solve the RANS equations fully coupled with the Spalart-Allmaras (SA) turbulence model. Specifically, SA-neg [64] is used with QCR2000 [65], and boundary layers are assumed to be fully turbulent.

D. Gradient-Based Optimization

Gradient-based optimization is performed using SNOPT [66], which can handle large-scale optimization problems subjected to linear and nonlinear constraints. For gradient evaluation, the discrete-adjoint method [67, 68] is used for objective function and constraint gradients that depend on the flow solution. For all other sensitivities, gradients are calculated either analytically or through the complex-step method [69].

C. Conceptual Design Problem Formulations

In this appendix, the conceptual design problem for each aircraft is presented, where the main objective is to develop representative aircraft concepts for the CTW160 and SBW160. Top level aircraft requirements are based on the Airbus A320neo, with a maximum payload of 44,100 lb, a design payload and design range of 165 passengers and 3,400 nmi, respectively, and a cruise Mach number of 0.78. The overall dimensions are also based on the Airbus A320neo, with

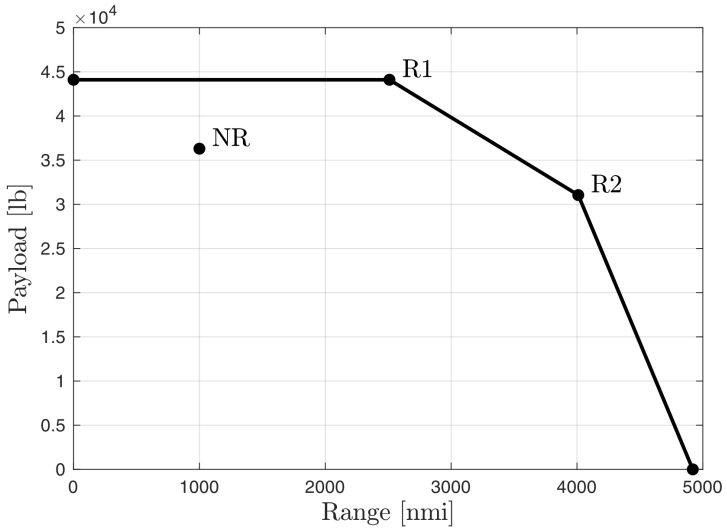

Fig. 20 Payload-range diagram based on the Airbus A320neo. The R1 and R2 design points are used to size each aircraft concept, while the nominal range (NR) mission is used to evaluate fuel burn performance.

Table 9 Reference engine data based on the Pratt and Whitney PW1127G.

Maximum thrust [lb]	20,860
Dry weight [lb]	4,800
Engine length [in]	187.0
Engine diameter (inlet) [in]	81.0
TSFC [lb/lbf/hr]	0.587

the exception of those related to aircraft components and subsystems unique to the strut-braced-wing configuration discussed later, which are based on the Boeing 765-095-RevD-DF and its Mach 0.80 variants [30].

The aircraft systems of each aircraft concept are sized based on the R1 and R2 design points of the payload-range diagram shown in Figure 20, which satisfy the design range mission requirements. These design points are derived from data provided in the airport planning manual of the Airbus A320neo [45], as well as notional reference data included in the CAEP 11 Independent Expert Integrated Review [70]. A nominal range mission is also considered, which represents a typically-flown mission used to evaluate the fuel burn performance of each aircraft concept. This results in an SBW160 with the same payload-range operating envelope as that of the CTW160, leaving a conceptual MDO problem with the objective of minimizing the block fuel required for completing the same nominal range mission.

The propulsion systems of each aircraft concept assumes two underwing mounted podded engines, which are modeled based on the Pratt & Whitney PW1127G [71]. Reference engine data is provided in Table 9, which is based on publicly available data, as well as notional reference data from the CAEP 11 report [70]. These reference parameters are used with the parametric models described in Appendix A to model the performance of each propulsion system.

Since the CTW160 is intended to represent the Airbus A320neo, it is modeled as-drawn based on publicly available

Table 10 Design variable information for the conceptual MDO of the SBW160.

Design Variable	Quantity	Bounds
Thickness-to-chord ratio, t/c	8	$0.8(t/c)_{\text{init}} \leq t/c \leq 1.5(t/c)_{\text{init}}$
Chord, c	8	$0.5c_{\text{init}} \leq c \leq 2.0c_{\text{init}}$
Horizontal tail chord, c_{h}	2	$0.5c_{\text{init}} \leq c_{\text{h}} \leq 2.0c_{\text{init}}$
Horizontal tail span, b_{h}	1	-5.0 ft $\leq b_{\text{h}} \leq +5.0$ ft
Horizontal tail x-location, x_{h}	1	-10.0 ft $\leq x_{\text{h}} \leq +10.0$ ft
Horizontal tail z-location, z_{h}	1	-10.0 ft $\leq z_{\text{h}} \leq +10.0$ ft
Vertical tail chord, c_{v}	2	$0.5c_{\text{init}} \leq c_{\text{v}} \leq 2.0c_{\text{init}}$
Vertical tail span, b_{v}	1	-5.0 ft $\leq b_{\text{v}} \leq +5.0$ ft
Vertical tail x-location, x_{v}	1	-10.0 ft $\leq x_{\text{v}} \leq +10.0$ ft
Maximum thrust, T_{max}	1	18,000 lb $\leq T_{\text{max}} \leq$ 28,000 lb
Initial cruise altitude, ICA	3	34,000 ft $\leq$ ICA $\leq$ 48,000 ft
Total	**29**	–

aircraft drawings and data [72]. For instance, the wing, fuselage, horizontal and vertical tails, nacelles, and pylons are modeled based on those of the reference aircraft, while the operating conditions are specified and maintained. The baseline sizing of the propulsion systems is also maintained to represent the Pratt & Whitney PW1127G. However, since wing thickness distributions are not readily available, design variables are included for the thickness-to-chord ratios at the wing centerline, root, crank, and tip. With these design variables, a minimum fuel volume constraint is included to help maintain sufficient wing volume and hence fuel capacity for storing the maximum usable fuel.

For the SBW160, design variables are included to size the wing, strut, horizontal and vertical tails, and propulsion systems, as well as for determining the optimal initial cruise altitude for the R1, R2, and nominal range missions. These design variables are accompanied by a wide range of geometric considerations and additional top level aircraft requirements that take the form of linear and nonlinear constraints, which help maintain the feasibility of the concept. An overview of the design variables and nonlinear constraints is provided in Tables 10 and 11, respectively.

For the wing and strut, design variables include thickness-to-chord ratio and chord design variables that are primarily driven by trades between aerodynamics and structures. These design variables define the wing system shown in Figure 21, which is modeled based on Gur et al. [17] and Meadows et al. [18]. Nonlinear constraints include minimum fuel volume, with fuel storage assumed to be available in the wing and strut; minimum buckling margins, which constrain wing segments 1, 2, and 3 during the $+2.5g$ load condition, and 4, 5, and 6 during the $-1g$ load condition; and maximum wing loading based on the Airbus A320neo, which places a minimum bound on the wing area of the aircraft for satisfying takeoff and landing requirements.

Linear constraints are also introduced to simplify the design of the wing system. These include constraints that maintain a constant chord over wing segments 1, 2, and 6 as per Chau and Zingg [35], a minimum tip chord of 3.5 ft

Table 11 Nonlinear constraints for the conceptual MDO of the SBW160.

Constraint	Qty	Bound	Description
Minimum fuel volume	1	–	Constrains the fuel storage capacity based on the maximum usable fuel, MFW
Maximum wing loading	1	131.1 lb/ft^2	Constrains the wing area based on a specified maximum MTOW/S_{ref}
Minimum thrust-to-weight ratio	1	0.311	Constrains the maximum takeoff thrust based on a specified T_{max}/MTOW
Minimum top-of-climb thrust	3	–	Constrains the thrust available at start of cruise to have sufficient excess for a 300 ft/min climb for each design mission
Minimum static margin	2	0.05	Constrains the static margin at the start and end of cruise for the nominal range mission
Minimum buckling margin	5	–	Ensures that any wing segment under compression across all load cases does not exceed the critical buckling load with a safety factor of 1.5
Minimum buffet margin	12	–	Constrains the relaxed drag divergence Mach number at four separate Mach-C_L points on the buffet envelope to not exceed the cruise Mach number; this buffet envelope analysis is performed separately for each design mission
Minimum horizontal tail volume ratio	1	1.571	Constrains the horizontal tail volume ratio
Minimum vertical tail volume ratio	1	0.070	Constrains the vertical tail volume ratio
Total	**27**	–	–

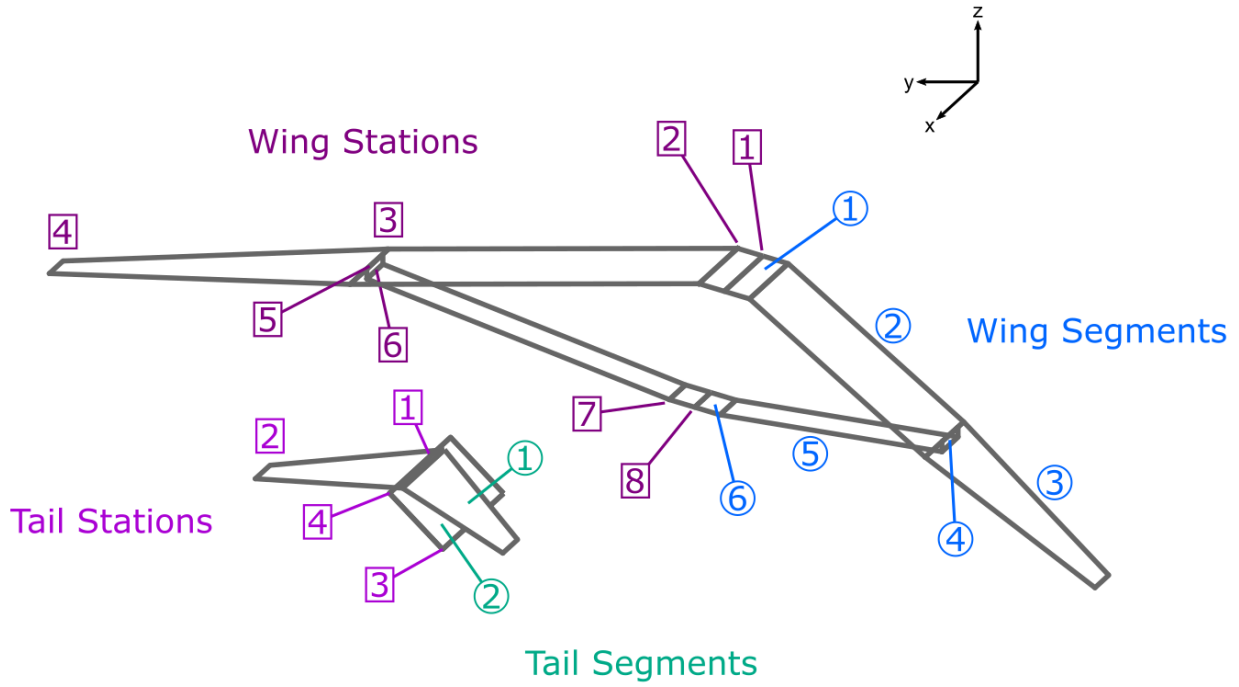

Fig. 21 Conceptual MDO.

based on the Boeing 765-095-RevD-DF [30], and a constant thickness-to-chord ratio and chord over the strut, i.e. wing segments 4, 5, and 6, based on References [17, 18]. A maximum bound of 0.12 is also imposed on the thickness-to-chord ratio of the strut, which is primarily driven by the buckling constraints. This is because the strut is assumed to be non-lifting during the conceptual design stage, and hence does not contribute to wave drag (see Appendix A). Although the Korn equation could still be used to approximate wave drag based on the thickness-to-chord ratio and sweep of each strut segment, these contributions are assumed to be negligible and generally too optimistic near the wing-strut junction, where large thickness-to-chord ratios can be expected to exacerbate the transonic interference effect.

Design variables such as sweep, span, and dihedral degrees of freedom are not included since they are assumed to exceed the modeling capabilities of the conceptual MDO framework. For example, the optimum wing span is highly sensitive to trades between aerodynamics and structures, and is often also driven by transonic aeroelastic effects such as flutter. Given that the conceptual MDO framework does not model transonic flutter, and its low-order models are considered insufficient for accurately resolving the aerostructural tradeoffs, wing span design variables are not included. Instead, these parameters are specified and maintained based on reference strut- and truss-braced-wing configurations.

In particular, a wing span of 153 ft is selected based on the Boeing 765-095-RevD-DF (with ICAC constraint) [30], which provides a 30% advantage over that of the Airbus A320neo. With the maximum wing loading constraint, this results in an aspect ratio close to the 17.15 of the Mach 0.80 variant of the Boeing SUGAR High [30] but at a reduced wing span, i.e. 153 ft compared to 162 ft, to compensate for the structural efficiency that would otherwise be provided

by jury struts. In order to accommodate the code C gate restrictions at 118 ft, a wing folding mechanism is included at approximately 77% semispan.

Since natural laminar flow, which prefers reduced leading-edge sweep angles to avoid crossflow instabilities at high Reynolds numbers [73], is not considered in the present work, a half-chord sweep angle of 30 degrees is selected to maximize wave drag performance at Mach 0.78. This decision, as well as the relative positioning of the wing and strut roots along the fuselage, which determine the sweep and dihedral angles of the strut, are based on the Mach 0.80 concept found in Bradley et al. [30]. The wing-strut junction is positioned at 55% semispan based on the Boeing SUGAR High [30], which is within the expected range of most strut- and truss-braced wing designs. This represents a reasonable tradeoff between load alleviation from the strut over the inboard portion of the wing, and higher axial loads through the strut when under compression.

For the horizontal and vertical tails, a T-tail configuration is assumed, as shown in Figure 21, which is based on the Boeing 765-095-RevD-DF [30]. To improve wave drag performance at Mach 0.78, however, the leading-edge sweep of the horizontal tail is increased from 25.6 degrees to 35.6 degrees based on the planforms presented in Harrison et al. [31]. In order to allow the tail system to be resized as changes are made to the wing design, the optimizer is allowed to vary the root and tip chords, and span of the horizontal and vertical tails. These design variables are primarily driven by minimum horizontal and vertical tail volume ratios based on the reference tail system, as well as constant taper and aspect ratios to help maintain similar levels of aerodynamic and structural performance. Design variables are also introduced to allow for changes to the location of the horizontal and vertical tails, which serve only to maintain the relative positioning of the tail surfaces based on the initial T-tail configuration. Thickness-to-chord ratios of 0.10 are assumed, with the horizontal tail featuring a dihedral angle of -3 degrees [30].

The initial cruise altitudes of the design missions are also included as design variables, which allow the optimizer to attain more optimal cruise lift coefficients for improving aerodynamic efficiency [37]. This provides the means for re-balancing the induced and viscous drag components at a given Mach number and wing loading. Since the objective is to minimize fuel burn, however, achieving a more optimal L/D through higher cruise altitudes must trade with increased climb and descent fuel, as well as other competing factors such as increased wave drag at higher cruise C_L values, and propulsion system sizing, as observed in Chau and Zingg [35].

It is important to note, however, that the wave drag approximations provided by the Korn equation can lead to optimistic estimates when considering combinations of high transonic Mach numbers and lift coefficients [74]. Although the method has been modified to include a penalty to the drag divergence Mach number for sectional lift coefficients ranging from 0.70 to 1.00 based on a linear interpolation of the data presented in Mason [75], early conceptual designs of the SBW160 still resulted in exceedingly high cruise C_L values. In part, this is due to the relatively high design wing loading of the SBW160, when compared to, for example, the transonic strut-braced-wing regional jet of Chau and Zingg [35]. To prevent this, a maximum cruise C_L of 0.750 is imposed based on the values considered in Harrison et

al. [31].

With regard to propulsion system sizing, the maximum takeoff thrust is included as a design variable to allow for changes to the thrust available at a given Mach number and altitude, while capturing trades with the weight and drag of the podded engines. This design variable is constrained by top-of-climb thrust requirements for each design mission, which demands sufficient excess thrust for achieving a 300 ft/min climb rate. Since the thrust available decreases with altitude, the optimizer must increase the overall size of the propulsion system in order to achieve a higher wing L/D. A minimum thrust-to-weight ratio constraint is also imposed based on the Airbus A320neo, which together with the maximum wing loading constraint, helps maintain takeoff and landing performance to first order.

As with Chau and Zingg [35], other nonlinear constraints include minimum buffet margins, which are based on a heuristic that helps maintain reasonable cruise C_L values, and minimum static margins at the start and end of cruise for the nominal range mission. A linear constraint is also included to match the initial cruise altitude of the R1 and R2 missions, which helps further simplify the design space.